

# Accepted Manuscript

## Small-Scale Variability in Saturn's Lower Ionosphere

Katia I. Matcheva, Daniel J. Barrow

PII: S0019-1035(12)00341-7

DOI: <http://dx.doi.org/10.1016/j.icarus.2012.08.022>

Reference: YICAR 10348

To appear in: *Icarus*

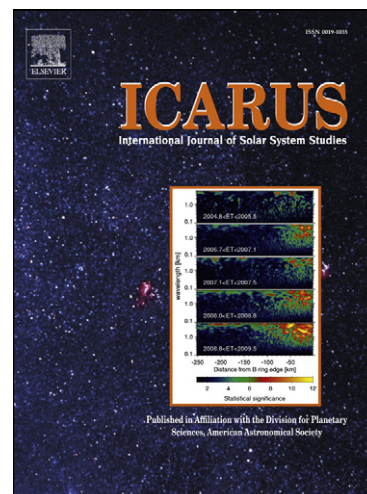
Received Date: 16 March 2012

Revised Date: 16 July 2012

Accepted Date: 16 August 2012

Please cite this article as: Matcheva, K.I., Barrow, D.J., Small-Scale Variability in Saturn's Lower Ionosphere, *Icarus* (2012), doi: <http://dx.doi.org/10.1016/j.icarus.2012.08.022>

This is a PDF file of an unedited manuscript that has been accepted for publication. As a service to our customers we are providing this early version of the manuscript. The manuscript will undergo copyediting, typesetting, and review of the resulting proof before it is published in its final form. Please note that during the production process errors may be discovered which could affect the content, and all legal disclaimers that apply to the journal pertain.



# Small-Scale Variability in Saturn's Lower Ionosphere

July 16, 2012

Katia I. Matcheva<sup>1</sup>

Daniel J. Barrow<sup>1,2</sup>

1 Department of Physics, University of Florida, Gainesville FL 32611-8440

katia@phys.ufl.edu

2 Buchholz High School, Gainesville FL 32606

barrowdj@gm.sbac.edu

## Corresponding Author:

Katia I. Matcheva

Department of Physics, University of Florida, P.O. Box 118440, Gainesville FL 32611-8440

e-mail: katia@phys.ufl.edu

phone: (352) 392 0286

**Abstract**

1  
2 We perform and present a wavelet analysis on all 31 Cassini electron density profiles  
3 published to date (Nagy et al., 2006; Kliore et al., 2009). We detect several discrete  
4 scales of variability present in the observations. Small-scale variability ( $S < 700$  km) is  
5 observed in almost all data sets at different latitudes, both at dawn and dusk conditions.  
6 The most typical scale of variability is 300 km with scales between 200 km and 450 km  
7 being commonly present in the vast majority of the profiles. A low latitude dawn/dusk  
8 asymmetry is noted in the prevalent scales with the spectrum peaking sharply at the  
9 300 km scale at dusk conditions and being broader at dawn conditions. Compared  
10 to dawn conditions the dusk ionosphere also shows more significant variability at the  
11 100 km scale. The 300 km vertical scale is also present in the few available profiles  
12 from the Northern hemisphere. Early observations from 2005 show a dominant scale at  
13 350 km whereas later in 2007-2008 the spectrum shifts to the shorter scales with the  
14 most prominent scale being 300 km. The performed wavelet analysis and the obtained  
15 results are independent of assumptions about the nature of the layers and do not require  
16 a definition for a "background" electron density profile.

17 In the second part of the paper we present a gravity wave propagation/dissipation  
18 model for Saturn's upper atmosphere and compare the wave properties to the char-  
19 acteristics of the observed electron density variability at different scales. The general  
20 features observed in the data are consistent with gravity waves being present in the  
21 lower ionosphere and causing layering of the ions and the electrons. The wave-driving  
22 mechanism provides a simultaneous explanation for several of the properties of the ob-  
23 served variability: (i) Lack of variability in the electron density above the predicted  
24 region of wave dissipation; (ii) In most cases the peak amplitude of variability occurs  
25 within the altitude range for dissipation of gravity waves or below; (iii) Shorter scales  
26 have smaller amplitudes than the longer scales; (iv) Shorter scales are present at lower  
27 altitudes whereas longer scales persist to higher altitudes; (v) Several layers often form  
28 a system of equally spaced maxima and minima that can be traced over a large altitude  
29 range.

30 **Keywords:** atmospheres, composition; atmospheres, dynamics; ionospheres; Saturn, atmo-  
31 sphere.

## 1 Introduction

Our current knowledge of the structure of the ionosphere of Saturn is based mostly on spacecraft radio occultations (Pioneer 10 and 11, Voyager 1 and 2, and Cassini) and observations of the auroral emission in the UV and the near IR. In addition, the detection and monitoring of the Saturn Electrostatic Discharges (SED) by the Voyager Planetary Radio Astronomy (PRA) experiment and by the Cassini Radio and Plasma Wave Science (RPWS) experiment carry information about the maximum electron density and its evolution with time (Warwick et al., 1981; Warwick et al., 1982; Fischer et al., 2006; Fisher et al., 2011). The thermal structure of the atmosphere at ionospheric heights is constrained by stellar and solar occultations performed by the Voyager UVS and the Cassini UVIS teams (Festou and Atreya, 1982; Smith et al., 1983; Nagy et al., 2009). The observations reveal an ionosphere with complex vertical structure which strongly varies with time and latitude (Nagy et al., 2006; Kliore et al., 2009).

Previous theoretical models of Saturn's ionosphere have focused on its overall structure (the maximum of the electron density and total electron content of the ionosphere) and its latitudinal and time dependence in an attempt to capture the main physics and chemical processes that control the ionosphere (Moore et al., 2010). Difficulties arise from the unconstrained abundance of vibrationally excited  $H_2$  molecules and the unknown amount of water influx from Saturn's rings, both of which are bound to have a strong impact on the ionospheric chemistry. Both quantities have been previously used as free parameters to reduce the lifetime of  $H^+$  ions and to decrease the predicted values for the maximum of the electron density in order to fit the observations (McElroy, 1973; Connerney and Waite, 1984; Majeed and McConnell, 1991, 1996; Moses and Bass, 2000; Moore et al., 2004). Furthermore, very little is known about the dynamics of Saturn's ionosphere since the available observations contain no direct information about the wind system at these altitudes. Doppler shifts in the  $H_3^+$  thermal emission lines can be used for measuring strong winds in Saturn's auroral region. In contrast to Jupiter, though, where thermospheric temperatures are in excess of 900 K, Saturn's  $H_3^+$  mid-to-low latitude emission has been difficult to detect even with the Cassini instruments (Melin et al. 2011).

61 The Cassini radio observations, resulting in 31 published electron density profiles to date,  
62 provide us with the most detailed picture so far of the structure of Saturn's ionosphere. The  
63 observations have been made during the first phase of the Cassini mission from 2005 to 2008,  
64 corresponding to southern hemisphere summer and early fall. The following features have  
65 been previously pointed out in the literature: 1) The maximum electron density as well  
66 as the total electron content (TEC) increase with latitude with a maximum in the polar  
67 regions (Moore et al., 2010). 2) At low latitudes the dawn electron density peak is smaller  
68 and occurs at higher altitudes (referred to as dawn/dusk asymmetry) (Nagy et al., 2006;  
69 Kliore et al., 2009). 3) A complex system of sharp layers of enhanced electron density is  
70 observed in the lower ionosphere at most latitudes. 4) Some profiles exhibit large vertical  
71 regions of near depletion of electrons (referred to as bite-outs).

72 In this paper we investigate the small-scale vertical layering present in a significant frac-  
73 tion of the 31 Cassini electron density profiles of Saturn published in the literature to date.  
74 Multiple layers in the electron density are observed in virtually all Cassini profiles as well as  
75 in the Voyager and Pioneer profiles although some of them do not extend to very low alti-  
76 tudes. The layers are seen in dusk and dawn conditions at low, mid and high latitudes. The  
77 number of identifiable layers, the magnitude of the electron density peaks, the vertical scale  
78 (thickness) of the layers, and the spacing between the individual peaks vary. In this paper  
79 we present a statistical analysis for the scale and the magnitude of the vertical variations  
80 present in the individual Cassini electron density profiles. The large number of observations  
81 allow us to study the spectrum of the vertical variability at different latitudes and to even  
82 compare dawn and dusk conditions.

83 It is well known that the terrestrial night-time ionosphere often displays similar systems  
84 of narrow layers of electrons which are usually attributed to atmospheric waves or plasma  
85 instabilities (Kelley, 1989). Similar layers have also been observed in the Galileo J0-ingress  
86 electron density profile of Jupiter which samples the ionosphere at dusk conditions (Hinson  
87 et al., 1997). This system of layers has been successfully modeled as a signature of an  
88 atmospheric gravity wave propagating in Jupiter's thermosphere (Matcheva et al., 2001;  
89 Barrow and Matcheva, 2011). The corresponding dawn electron density profile of Jupiter  
90 however showed very different ionospheric structure with no well pronounced small-scale

91 layers.

92 In the second part of this paper we model the propagation of atmospheric gravity waves  
93 in Saturn's thermospheric/ionospheric region and compare the predicted properties of the  
94 waves to the spectral characteristics of the observed variability in the electron density.

## 95 2 Vertical variability in the electron density

96 The first step in our analysis is to study the variability in the data with minimum theo-  
97 retical assumptions about the nature of the fluctuations and/or the state of the ionosphere.  
98 We perform a wavelet analysis on all 31 electron density profiles published to date by the  
99 Cassini Radio Science Team to identify the prevalent scales of variability in the vertical elec-  
100 tron density distribution. A brief mathematical introduction to the theory and application of  
101 the wavelet analysis can be found in Torrence and Compo (1998) along with a downloadable  
102 software for public use. For the purpose of our study we use the continuous wavelet transform  
103 together with the Morlet wavelet basis as it provides us with optimal scale discrimination  
104 and vertical resolution. For a discrete series of measurements,  $x_n$ , ( $n = 0 \dots N - 1$ ), with equal  
105 spacing  $\delta t$  (in our case the sampling is done in space rather than in time) the functional form  
106 of the Morlet wavelet is

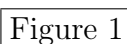
$$\psi_0(\eta) = \pi^{-1/4} e^{i\omega_0\eta} e^{-\eta^2/2}, \quad (1)$$

107 where  $\eta = \frac{n\delta t}{S}$  is a dimensionless "time" parameter,  $\omega_0$  is the dimensionless frequency, and  
108  $S$  is a scale of variability (analogous to the wavelength in a Fourier transform). The Morlet  
109 function is essentially a cosine function multiplied with a Gaussian. The frequency  $\omega_0$  reflects  
110 the number of oscillations within the Gaussian envelope. In this study we use  $\omega_0 = 6$   
111 which assures that the wavelet function has enough vanishing moments and can resolve high  
112 frequency signals.

113 The wavelet coefficients  $W_n(S)$  for a given scale  $s$  and position  $n$  are then calculated  
114 using the continuous wavelet transform

$$W_n(S) = \sum_{n'=0}^{N-1} x_{n'} \psi_0^* \left[ \frac{(n' - n)\delta t}{S} \right], \quad (2)$$

115 where (\*) indicates a complex conjugate. Similar to the Fourier coefficients the square of  
 116 the wavelet coefficients presents the energy within a given scale of variability. In many cases  
 117 the wavelet analysis is a preferred tool for data analysis as it also shows how the magnitude  
 118 of these variations changes within the length of the data set. In our analysis the calculated  
 119 wavelet coefficients (2) are normalized so that the square of the wavelet coefficient is equal  
 120 to the square of the amplitude of the observed variation rather than the power of the present  
 121 scales.

122  Figure 1

123  Figure 2

124  Figure 3

125  Figure 4

126 The results from the wavelet analysis for selected latitudes are shown in Figs. 1-4. The  
 127 results for the remaining 27 cases are shown in the Appendix in Figs. A.1-A.27. Figure  
 128 1 shows the analysis of a high latitude observation (72°S at dusk), Fig. 2 presents a mid  
 129 latitude case (28°S at dusk), Figs. 3 and 4 correspond to low latitude conditions at dusk  
 130 (3°S) and dawn (9°S), respectively. The choice of latitudes is to illustrate the fact that  
 131 layering in the ionosphere of Saturn is present at all latitudes at diverse local conditions and  
 132 time of the day.

133 Each of the figures has three panels showing the local electron density profile (left panel),  
 134 a color map of the variations  $Re(W_n(S))$  present in the data at different scales as a function  
 135 of altitude (central panel), and a color map of the amplitude of the variations  $|W_n(S)|$  at  
 136 different scales as it changes with height (right panel). The variations  $N'_e$  are normalized  
 137 to the peak electron density,  $N_{e,max}$ , and the result  $\frac{N'_e}{N_{e,max}}$  is presented in percentage. By  
 138 definition the variation cannot exceed 50% . The contours are drawn at 5% intervals. A  
 139 vertical slice through the amplitude color map shows how the amplitude at a given scale  $S$   
 140 changes with height. A horizontal cut through the map at a given altitude produces the  
 141 spectrum of the scales present at this height. Similar to the Fourier analysis the wavelet

142 analysis suffers from edge effects. The effect is scale dependent and results in distortion of  
 143 the power at the edge of the map at a distance one scale length away from the edge.

144 Figure 5

145 To answer the question, how significant are the scales identified in Figs. 1-4 we present  
 146 the wavelet analysis of S56 exit occultation together with a contour of the 5% significance  
 147 level as defined by Torrence and Compo (1998) (Fig. 5). The calculation is based on the  
 148 variance in the observed electron density profile and assumes a white power-spectrum for the  
 149 noise. The 5% significance level is equivalent to the 95% confidence level tested against a  
 150 white noise background. One can see that the 5% significance level in Fig. 5 closely mimics  
 151 the 5% contour in Fig. 1 and includes all identified features.

152 At this point the wavelet analysis is performed without any assumption about the nature  
 153 of the layers and the origin of the vertical variability. There is no predefined "background"  
 154 ionospheric state. This is reflected in the presence of significant power at very large scales  
 155 ( $S > 800$  km) which are likely to represent the overall structure of the ionosphere resulting  
 156 from ion chemistry and diffusion. The wavelet analysis provides information about the  
 157 dominant scales of variability in the data, the amplitude of the fluctuations and how this  
 158 amplitude varies with height. The last point makes the wavelet analysis particularly valuable  
 159 in studying altitude dependent periodic phenomena. A summary of the wavelet results  
 160 (detected scales  $S$ , maximum amplitude  $\Delta N_{e,max}$ , peak altitude  $Z_{max}$ ) presented in Figs. 1  
 161 through 4 is shown in Table I.

162 Table I

163 The analysis of the high latitude S56 exit electron density profile (Fig. 1) reveals vari-  
 164 ability at several different scales. As we discuss earlier the strong power contained at large  
 165 scales ( $S = 900$  km) reflects the overall structure of the ionosphere. Three shorter scales  
 166 ( $S=165$  km, 250 km, and 500 km) are also evident in the wavelet amplitude map. Individual  
 167 trains of several peaks can be clearly traced in the wavelet coefficient map (Fig. 1 center).  
 168 The amplitude of the 500 km scale has a very broad peak in the altitude range between 700

169 km and 1800 km (Fig. 1 right). At the 165 km scale the maximum variability is at 1200 km  
170 and for the 250 km scale the amplitude is maximum at the 1000 km altitude level.

171 The analysis of the midlatitude dusk profile presented in Fig. 2 shows strong variability  
172 at a scale of 450 km, which peaks at an altitude of 1350 km. A second, shorter scale at 210  
173 km can be traced in the wavelet map with much smaller amplitude that reaches a maximum  
174 at about 1000 km.

175 The dusk and dawn low latitude profiles shown in Figs. 3 and 4 also exhibit strong  
176 layering at the bottom of the ionosphere. The S08 entry profile is dominated by a single  
177 scale of variability ( $S=380$  km) which corresponds to the three dramatic peaks visible in the  
178 electron density profile. The layers in the S07 exit observation are more subtle but one can  
179 clearly identify the individual peaks in the 360 km scale as high as 2500 km above the 1 bar  
180 pressure level. A 570 km scale can be identified in the wavelet map as well, though it is too  
181 close to the bottom boundary of the analyzed region and might be distorted by edge effects.

182 As each electron density profile is different and every one of them provides a clue about the  
183 nature of the variability we present the wavelet analysis of all remaining 27 electron density  
184 profiles in the Appendix for the benefit of the reader. Based on the wavelet analysis of all  
185 31 occultations we can make the following observations: (i) Multiple layers are present at all  
186 latitudes both at dusk and dawn conditions. (ii) Large amplitude variability and layering is  
187 more common in the lower ionosphere (below and at the main electron density peak) though  
188 small amplitude variation in the electron density is sometimes present throughout the entire  
189 observed altitude range (see for example occultation S11 exit, Fig. A.6). (iii) Longer scales  
190 tend to persist up to higher altitudes and have larger amplitudes than shorter scales. (iv)  
191 A number of profiles exhibit 2-3 dramatic equally spaced sharp layers (S68 entry, Fig. 2)  
192 while other profiles have embedded small-amplitude electron density variations which one  
193 can trace in the data for several cycles over a long distance (S07 exit, Fig. 4). (v) In a  
194 few cases the layers of electrons are separated by regions that are completely depleted of  
195 electrons (S47 exit, Fig. A.15).

196

Figure 6

197

Figure 7

198 To illustrate the full diversity of scales detected in the Cassini electron density profiles  
 199 we present a statistical summary of the results from the wavelet analysis of all 31 profiles.  
 200 Figure 6 shows the fraction of profiles in which a scale  $S$  is detected with an amplitude larger  
 201 than 5%. The scales are grouped in bins of  $\Delta S = 50$  km and range from  $S = 50$  km to  
 202  $S = 1000$  km. Note that the smallest scale used in the wavelet analysis is 16 km; however, no  
 203 significant power is detected at scales smaller than 50 km. To search for latitudinal trends we  
 204 present similar histograms after sorting the observations into "high latitude", "mid latitude"  
 205 and "low latitude". One can also compare dawn and dusk conditions. The results are shown  
 206 in Fig. 7, where we consider low latitude profiles only. The counts are normalized by the total  
 207 number of available profiles: 8 for dusk and 8 for dawn conditions. In contrast to a power  
 208 spectrum the presented histograms do not contain information about the magnitude of the  
 209 variations. They simply reflect the frequency of occurrence of a given scale of variability  
 210 with an amplitude in excess of 5%. Based on the histograms one can make the following  
 211 conclusions:

212 1) Overall the most typical scale of vertical variability is 300 km. Only three out of the  
 213 31 profiles show no fluctuations at scales less than 450 km. The scale values are approximate  
 214 as the width of the bins is 50 km.

215 2) The midlatitudes are dominated by 300 km variability whereas at low latitudes the  
 216 350 km scale prevails. High latitudes show a broad range of scales shorter than 500 km.

217 3) At low latitudes the dusk ionosphere most often shows the presence of a 300 km scale  
 218 and the frequency of occurrence of 250 km and 350 km scales is reduced by half in comparison  
 219 to dawn observations.

220 4) There is a significant variability at the 100 km scale, however, the amplitude of the  
 221 fluctuations are typically less than the 5% cutoff and the variability is confined to the very  
 222 bottom of the observed region. The 100 km scale is most notable at low latitudes at dusk  
 223 conditions.

224

Figure 8

225 The analyzed observations are done over a time period of a few years starting in 2005  
 226 through 2008. It is reasonable to expect that the spectrum of the present scales might evolve

227 in time over the years. We compare the observations made in 2005 with the observations  
228 made later in the mission (late 2007-2008). The corresponding histograms are shown in  
229 Fig. 8. The 2005 observations are done within 4 months and are exclusively at low latitudes.  
230 The second group of observations (2007-2008) are from high and middle latitudes and one  
231 low latitude. A few observations are made in 2006 or early 2007. Since they are significantly  
232 separated in time from the other two groups we do not include them in this analysis. With  
233 this time selection the scatter in the histograms in Fig. 8 is decreased and we see a dominant  
234 350 km scale for the 2005 low latitude observations and a dominant 300 km for the 2007-2008  
235 observations. Although the shift towards shorter scales is well pronounced one should keep  
236 in mind that the size of the histogram bins is 50 km and the shift is within the uncertainties  
237 of the analysis. It is also possible that the shift reflects the difference in the sampled latitudes  
238 rather than a real seasonal change.

239 Finally most of the observations in our analysis are from the southern hemisphere with  
240 only 5 electron density profiles from the northern hemisphere. At this point one cannot  
241 make any statistical comparison based on hemispheric separation except to note that the  
242 electron density profiles in the northern hemisphere also have sharply peaked layers in the  
243 lower ionosphere with the 300-350 km scale present in all five of the profiles (see Appendix  
244 Figs. A.4 , A.7, A.12, A.24, and A.26). It would be interesting to extend this statistical  
245 analysis to the northern hemisphere as new observations become available.

### 246 3 Atmospheric Gravity Waves

247 The wavelet analysis in Section 2 demonstrates the presence of a wide range of scales of  
248 variability in the electron density profiles which give rise to the layered appearance of Saturn's  
249 lower ionosphere. The question about the origin of these layers is open for discussion. In  
250 this paper we investigate the hypothesis that the observed small-scale layering is caused by  
251 atmospheric gravity waves that propagate into Saturn's upper atmosphere.

252 Atmospheric gravity waves are buoyancy driven oscillations of a parcel of air which in a  
253 stable atmosphere can propagate over a large distance. In contrast to sound waves, gravity  
254 waves are transverse waves with frequencies smaller than the buoyancy frequency of the at-

255 mosphere. On the other hand the period of a gravity wave is smaller than the period of a  
 256 typical Rossby wave so that the planetary rotation does not significantly impact its propa-  
 257 gation. The dispersion relation for a hydrostatic gravity wave in a conservative atmosphere  
 258 is given by:

$$k_z^2 = \frac{k_h^2 N^2}{\omega^2} - \frac{1}{4H^{*2}}, \quad (3)$$

259 where  $k_z$  and  $k_h$  are the vertical and the horizontal wave numbers, respectively,  $N$  is the  
 260 buoyancy frequency,  $H^*$  is the atmospheric density scale height, and  $\omega$  is the wave frequency.

261 Atmospheric gravity waves are easily excited by transient atmospheric phenomena, at-  
 262 mospheric instabilities, weather fronts, convective storms, etc. In a conservative atmosphere  
 263 with no wind shear the amplitude of the waves grows exponentially with altitude as the  
 264 background density decreases with height. As a result small-amplitude waves generated in  
 265 the lower atmosphere can attain large amplitudes by the time they reach the thermosphere  
 266 and can leave observable signatures in the temperature structure and the wind profile of  
 267 the atmosphere at these heights. Not all gravity waves make it to very high altitudes (low  
 268 pressure levels) as they are subject to a number of dissipative processes. Along their path  
 269 they might get absorbed in the mean zonal wind or reflected by strong temperature gradi-  
 270 ents. Waves with amplitudes that are big enough to drive the local temperature gradient  
 271 beyond the dry adiabatic lapse rate become unstable and overturn, depositing energy and  
 272 momentum in the background atmosphere. In addition, waves that reach low pressure levels  
 273 are dissipated by diffusive processes like molecular viscosity and heat conduction. For a  
 274 detailed mathematical treatment of wave propagation and dissipation we refer the reader to  
 275 Hines (1974), Lindzen (1981), and Walterscheid (1981).

276 In our work we use an atmospheric gravity wave model that is based on the assumptions  
 277 that the waves are linear and hydrostatic, that the atmospheric temperature is slowly varying  
 278 with height and that the vertical gradient of the mean zonal wind is zero. The model includes  
 279 wave dissipation due to molecular viscosity, eddy diffusion, and thermal conduction. We keep  
 280 the amplitude of the waves below the breaking point at all heights. The model has been  
 281 originally developed for Jupiter and subsequently adapted for Saturn. The mathematical  
 282 details and the numerical implementation of the model are presented in Matcheva and Strobel  
 283 (1999) and Matcheva et al. (2001) and summarized below. A single linear wave is imposed

284 at the bottom of the simulated region ( $z_0$ ) by defining the wave vertical and horizontal  
 285 wavenumbers ( $k_{z0}$  and  $k_h$ , respectively), vertical velocity amplitude  $\Delta W(z_0)$  and phase. We  
 286 then solve the dispersion equation Eq. (4) for the complex and real parts of the vertical  
 287 wavenumber ( $k_z = k_{zr} + ik_{zi}$ ), and the amplitude of the resulting vertical  $\Delta W(z)$  and  
 288 horizontal  $\Delta V(z)$  velocity fields as the wave propagates up in the atmosphere (Eqs. (5) and  
 289 (6)).

$$k_z^2 = \frac{k_h^2 N^2}{\tilde{\omega}(\tilde{\omega} + i\beta)} - \frac{1}{4H^{*2}} \left[ 1 - 2 \frac{dH^*}{dz} \right] \quad (4)$$

$$\Delta W(z) = \Delta W(z_0) \left( \frac{k_{zr0}}{k_{zr}} \right)^{1/2} \exp \left[ \int_{z_0}^z \left( \frac{1}{2H^*} - k_{zi} \right) dz \right] \quad (5)$$

$$\Delta V(z) = \Delta W(z) \left( \frac{k_{zr}}{k_h} \right) \sqrt{1 + \left( \frac{k_{zi}}{k_{zr}} + \frac{1}{H^* k_{zr}} \right)^2} \quad (6)$$

292 In Eq. (4)  $\tilde{\omega}$  is a complex frequency with a real part corresponding to the wave's actual  
 293 frequency and a complex part resulting from the viscous dissipation,  $\beta$  is a dissipation factor  
 294 representing the effect of thermal conductivity. The analytical definitions for  $\tilde{\omega}$  and  $\beta$  are  
 295 given in Matcheva et al. (2001). The bottom boundary of the model is at  $z_0 = 500$  km and  
 296 the top boundary is placed at 2500 km above 1 bar pressure level. The vertical step of the  
 297 calculations is 1 km. A subscript 0 is used to refer to parameters specified at the bottom of  
 298 the modeled region  $z_0$ .

## 299 4 Structure of the neutral atmosphere

300 The background neutral atmosphere used for the wave model is horizontally homogeneous  
 301 with no winds. The vertical structure is summarized in Fig. 9. Similar to Jupiter the  
 302 dominant neutral species in Saturn's atmosphere are  $H_2$ ,  $He$ , and  $CH_4$  with atomic hydrogen  
 303 becoming important at high altitudes. Below the methane homopause (around 900 km above  
 304 the 1 bar pressure level) eddy diffusion dominates and the atmosphere is well-mixed. The  
 305 eddy diffusion coefficient incorporated in the model varies with height and is taken from  
 306 Moses et al. (2000). Above the homopause, where molecular diffusion is dominant, the  
 307 species separate diffusively according to their individual scale heights and the  $CH_4$  and  $He$   
 308 mixing ratios decrease quickly with altitude.  $H_2$  is dominant up to roughly 3000 km at which

309 point  $H$  becomes the main neutral component. The neutral densities are calculated using  
310 the mixing ratios for  $He$  and  $CH_4$  at the bottom boundary of the model and are taken from  
311 Conrath and Gautier (2000). The resulting neutral density profiles are in good agreement  
312 with the composition model from Moses and Bass (2000). The background neutral winds  
313 are set to zero throughout the simulations.

314 Figure 9

315 The choice of temperature profile is essential for modeling atmospheric gravity waves as  
316 the wave propagation is impacted by the thermal structure through the buoyancy frequency  
317 (see Eq. 3). In addition, the environmental lapse rate controls the maximum amplitude for  
318 a given vertical wavelength before the wave becomes unstable and overturns.

319 The thermal structure of Saturn's troposphere and lower stratosphere is well constrained  
320 by Cassini CIRS observations (Fletcher et al., 2010). Middle stratospheric regions are ac-  
321 cessible by ground based stellar occultations (Hubbard et al., 1997; Harrington et al., 2010)  
322 whereas the upper stratosphere and lower thermosphere have been sampled by the Voyager  
323 and Cassini stellar and solar occultations (Festou and Atreya, 1982; Smith et al., 1983; Lindal  
324 1992). The CIRS temperature maps of the lower stratosphere show the temperature at the 1  
325 mbar level to vary by more than 30 K from pole to pole. The number of temperature profiles  
326 in the upper stratosphere and thermosphere are limited, they have significant uncertainties  
327 (about 100 K), and show large variability (Nagy et al., 2009). Temperature estimates at the  
328 top of the thermosphere vary from 300 K to 500 K (Nagy et al., 2009). In view of these  
329 uncertainties we use a generic temperature profile shown in Fig. 9 which captures the main  
330 observed features: a relatively isothermal stratosphere at  $T = 137$  K at the bottom of the  
331 modeled region, followed by a fast temperature increase between 800 km and 1300 km and  
332 topped by an isothermal layer at  $T = 417$  K. This temperature profile closely follows the T  
333 profile compiled by Moses et al. (2000). Subsequently we keep in mind that the temperature  
334 in the thermosphere is likely to vary from latitude to latitude as well as with time.

## 5 Propagation and dissipation of atmospheric gravity waves

In this section we address the question if and what type of gravity waves can reach the altitude region of interest (500-2500 km above 1 bar level) and what are the observational constraints on the wave parameters. As we discuss in Sec. 3, not all gravity waves can reach the upper atmosphere. They can be absorbed, reflected or dissipated as they travel through the lower atmosphere. Undoubtedly the wind system in the stratosphere has a strong filtering effect on the tropospheric waves which can reach the ionosphere. At this point, however, we do not know the origin of the waves, nor the wind system in the upper stratosphere. Instead we focus on the ability of the waves to overcome dissipative processes like eddy and molecular viscosity and thermal conduction that dominate wave dynamics at high altitudes. These dissipative processes are selective as waves with longer vertical wavelengths and shorter periods (see Eq. 4) tend to be less impacted by the molecular dissipation and can propagate higher in the atmosphere.

Figure 10

Figure 10 illustrates the behavior of the amplitude (vertical velocity, horizontal velocity, and temperature) of three atmospheric gravity waves together with a profile of the vertical wavelength as the waves pass through the modeled region. The three waves have a period of 30 min and vertical wavelength at the bottom of 50 km, 100 km, and 200 km respectively. In agreement with Eq. (5), the vertical velocity amplitude peaks at an altitude where dissipation overcomes the natural exponential growth of the wave:

$$k_{zi} = \frac{1}{2H^*}. \quad (7)$$

We refer to this altitude as the altitude of wave dissipation ( $z_d$ ), though the dissipation occurs in a rather broad altitude range and not just at this particular location. Above this altitude the magnitude of the observable signature of the wave is decreasing as the amplitude becomes smaller. The wave with the longest vertical wavelength has the highest dissipation altitude as the periods of the waves are the same. In contrast to the vertical velocity the amplitude of the horizontal velocity of the 100 and the 200 km waves has two peaks (Fig. 10b,c). The top one marks the region where the dissipation becomes dominant whereas the bottom peak

362 results from the variation of the background temperature and the subsequent changes in  
 363 the atmospheric stability. The bottom peak or hump is at the same altitude for waves of  
 364 all scales ( $z = 1100$  km) whereas the location of the top peak is scale-dependent. Figure  
 365 10 also shows the variation of the vertical wavelength with height. The vertical wavelength  
 366 changes significantly in the 900-1200 km region as a result of the fast temperature change  
 367 at the homopause. A variable vertical wavelength together with a double-peaked amplitude  
 368 profile can be an indication for a strong temperature gradient in the background atmosphere.  
 369 However, this is not a unique interpretation as varying background winds can have a similar  
 370 effect on the wave propagation.

371 Figure 11

372 Figure 11 shows the altitude of wave dissipation  $z_d$  for a range of vertical wavelengths  
 373 and periods. We consider vertical wavelengths less than 700 km to comply with the WKB  
 374 approximation of our gravity wave model and periods between the buoyancy period ( $\tau =$   
 375  $2\pi/N$ ) and one Saturnian day ( $\sim 10$  h). Each curve corresponds to a family of waves  
 376 with the same period ranging from 30 min (top curve) period to 10 hours (bottom curve)  
 377 in increments of 10 min. Waves with large vertical wavelengths and short periods (larger  
 378 frequency) dissipate high in the atmosphere. Figure 11 shows that waves with a vertical  
 379 wavelength shorter than 100 km reach a maximum amplitude at altitudes below 1200 km  
 380 even for the highest frequencies (period of 30 min). This implies that gravity waves can not  
 381 cause significant electron density layering with a characteristic vertical scale less than 100 km  
 382 at an altitude above 1300 km. Similarly one can state that waves with vertical wavelength  
 383 of 300 km reach a maximum amplitude at or below 1600 km. Above 1900 km gravity waves  
 384 should not cause strong observable signatures with a characteristic scale of 300 km.

385 Figure 11 also shows that at large periods the dissipation height  $z_d$  is only weakly de-  
 386 pendent on the wave period, or in other words for a given vertical wavelength waves with a  
 387 period between 0.5 and 1 Saturn day peak at roughly the same altitude.

388 The dissipation curves for gravity waves with a period of 30 min and 10 h are plotted  
 389 on the wavelet coefficient maps for all 31 electron density profiles presented in Figs. 1-4 and  
 390 in the remaining figures in the Appendix as light solid lines A and B, respectively. The

391 curves can be used as a guide for the range of altitudes where gravity wave signatures can  
 392 be expected. Roughly one wavelength above line A gravity waves are not expected to cause  
 393 strong variability in the electron density profile. The best gravity wave candidates would  
 394 have a signature in the electron density that is maximum in the region between curves A and  
 395 B. A local maximum in the wavelet map below curve B is still consistent with a gravity wave  
 396 interpretation. The peak can be caused by background temperature variation and/or local  
 397 ion chemistry which can modify the response of the ionosphere to the forcing neutral wave.  
 398 In this case the dissipation altitude of the wave  $z_d$  does not coincide with the maximum of  
 399 the electron density variability.

## 400 6 Discussion

401 In Sec. 2 we analyze the variability of the electron density profiles for characteristic  
 402 vertical scales and in Sec. 5 we describe the propagation/dissipation of gravity waves in  
 403 the upper atmosphere. Here we will discuss how compatible the observed variations in the  
 404 electron density profiles are with gravity wave signatures. We focus on vertical scales shorter  
 405 than 700 km with amplitudes larger than 5% in the wavelet maps presented in the Appendix  
 406 and in Figs. 1-4. While discussing the observed features one should keep in mind that the  
 407 wave model that we use relies on a generic temperature profile which is kept constant for  
 408 all latitudes and atmospheric conditions (dawn/dusk for example). Almost certainly the  
 409 temperature behavior varies from location to location and in time and therefore the exact  
 410 wave propagation would also vary. Nevertheless we can make the following observations:

411 • *Multiple layers with a vertical scale less than 700 km are present in most observation*  
 412 *at all latitudes both at dusk and dawn conditions.* Noted exceptions are S47 exit, S54 exit,  
 413 and S70 exit where the variability is at larger scales.

414 This is consistent with a gravity wave driving mechanism. Gravity waves are easily gener-  
 415 ated and can propagate over long distances in Saturn's stable middle and upper atmosphere.  
 416 Small amplitude waves generated in the troposphere can become large and well observable  
 417 by the time they reach the ionosphere.

418 • *There is no strong variability (amplitude > 5%) at any scale shorter than 700 km above*

419 *line A*. Noted exceptions are the equatorial observations S07 exit, S11 exit, S12 exit, S13  
420 exit, S44 entry, and the only north high latitude profile S46 exit.

421 This is consistent with a gravity wave driving mechanism. Line A shown in the wavelet  
422 amplitude maps provided in the Appendix indicates the altitude at which a 30 min wave  
423 peaks for different vertical wavelengths. The 30 min time scale corresponds to the buoyancy  
424 frequency at high altitudes ( $>1300$  km). This is the shortest gravity wave period to be  
425 expected at this altitude. The buoyancy period at the homopause is about 15 min.

426 • *In general, smaller scales of variability are present at lower altitudes whereas larger*  
427 *scales persist to higher altitudes.* Exceptions are S07 exit, S10 exit, S11 exit, and S13 exit.

428 This is also consistent with a gravity wave driving mechanism. As discussed in Sec. 5  
429 waves with short vertical wavelengths dissipate at lower altitudes whereas waves with large  
430 vertical wavelengths reach high altitudes before they become impacted by dissipation. The  
431 wavelet amplitude maps clearly show a trend of larger scales being present at higher altitudes.

432 • *Smaller scales have smaller amplitudes whereas larger scales reach much larger ampli-*  
433 *tudes.*

434 This is consistent with a gravity wave driving mechanism. The gravity wave amplitude  
435 growth is limited both by dissipation and by atmospheric instabilities. The linear wave  
436 theory predicts that gravity waves become unstable and overturn when the local temperature  
437 gradient exceeds the dry adiabatic lapse rate. Waves with shorter vertical wavelengths are  
438 associated with larger vertical gradients and are therefore prone to instabilities at small  
439 amplitudes. As a result waves with large vertical wavelengths are allowed to grow to larger  
440 amplitudes as they propagate up in the atmosphere.

441 • *In many cases there are several layers with the same vertical scale resembling a wave-*  
442 *train at a fixed wavelength.*

443 This is consistent with a gravity wave driving mechanism. Although forming layers of  
444 enhanced electron density is not restricted to the gravity wave mechanism only, what is  
445 specific for the proposed mechanism is the equal spacing between the individual layers (a  
446 relatively constant vertical wavelength) and the multiplicity of the layers (the wave can be  
447 traced over several wavelengths as the wave train propagates). This is especially true for  
448 the smaller-scale, small-amplitude variability detected in the data (see for example S07 exit

449 and S56 exit).

450 • *In most cases the peak amplitude occurs within the altitude range for a typical gravity*  
451 *wave dissipation (between lines A and B) or below.*

452 This is consistent with a gravity wave driving mechanism. The region bracketed between  
453 lines A and B in the wavelet maps corresponds to the dissipation altitude for waves with  
454 periods between 30 min and 10 hours. In general one can use the location of the observed  
455 wave amplitude peak to constrain the wave frequency and horizontal wavelength for a given  
456 vertical wavelength using Eq. (3) and (7). However, the observed parameter in the Cassini  
457 radio occultations is the variability in the electron density rather than in the temperature  
458 or in the wind of the neutral atmosphere. The response of the ionosphere to gravity wave  
459 forcing is indeed proportional to the neutral wave amplitude but this is not the only factor  
460 that shapes up the amplitude of the induced electron density variations. The magnitude  
461 of the effect is limited by local chemistry and modified by the electron density gradient in  
462 the background ionosphere (Matcheva et al., 2001; Barrow and Matcheva, 2011; Barrow et  
463 al., 2012). The bottom line is that without a careful modeling of the wave-ion interaction and  
464 local ion chemistry one cannot predict the location of the peak electron density variability  
465 in response to a given wave forcing. Such models exist for Jupiter (Matcheva et al., 2001;  
466 Barrow and Matcheva, 2011) and are under development for Saturn (Matcheva and Barrow,  
467 in preparation). This prediction is particularly difficult for large-amplitude variations where  
468 the variability is of the order of the average electron density and linear perturbation models  
469 are inadequate to describe the interaction between the ions and the propagating gravity  
470 wave.

## 471 7 Conclusions

472 We perform a wavelet analysis on all Cassini electron density profiles published to date  
473 (Nagy et al., 2006; Kliore et al., 2009). The results are shown in the Appendix. We detect  
474 several discrete scales of variability present in the observations. Small-scale variability ( $S <$   
475  $700$  km) is observed in almost all data sets at different latitudes and dawn/dusk conditions.  
476 The most typical scale is 300 km but scales between 200 km and 450 km are commonly present

477 in the vast majority of the profiles. A dawn/dusk asymmetry is noted in the prevalent scales  
478 with the most often observed scale being 200 km at dawn and 300 km at dusk. Compared  
479 to dawn conditions the dusk ionosphere also shows more significant variability in the 100 km  
480 scale. The 300 km vertical scale is also present in the few available profiles from the Northern  
481 mid and high latitudes. The performed wavelet analysis is independent of assumptions about  
482 the nature of the layers and does not require a definition for the "background" electron  
483 density profile and thus the results can be used independently of our wave interpretation of  
484 the origin of the variability.

485 In the second part of the paper we present a gravity wave propagation/dissipation model  
486 for Saturn's upper atmosphere and compare the wave properties to the characteristics of the  
487 observed electron density variability at different scales. The general features observed in the  
488 data are consistent with gravity waves being present in the lower ionosphere and causing  
489 layering of the ions and the electrons. Though this is not a unique interpretation, the wave-  
490 driving mechanism provides simultaneous explanation for several of the properties of the  
491 observed variability: lack of layers above the region of wave dissipation; the scale-dependent  
492 altitude of the layers; the scale-dependent magnitude of the layers; the observed altitude  
493 range of maximum variability in the ionosphere.

494 An exact match to an observed electron density profile with a wave model requires a  
495 careful modeling of Saturn's ionosphere (both chemistry and dynamics) and is currently  
496 underway.

## 497 Appendix

498 The results from the wavelet analysis of all individual Cassini electron density profiles  
499 of Saturn that are published to date are presented here in chronological order starting with  
500 S07 entry in 2005 (Fig. A.1) and finishing with S75 exit in 2008 (Fig. A.27) . The format of  
501 the plots is the same as in Fig. 1. The Discussions (Sec. 6) and the Conclusions (Sec. 7) in  
502 this paper are based on the results presented in these figures.

503

Figures A.1 to A.27

## Acknowledgments

The authors thank Dr. A. J. Kliore for providing the electron density profiles for Saturn obtained by the Cassini Radio Science Experiment. We also thank the ISSI International Team on Saturn Aeronomy (number 166) for the helpful discussions.

## References

1. Barrow, D. and Matcheva, K. I., 2011. Impact of atmospheric gravity waves on the jovian ionosphere. *Icarus* 211, 609-622.
2. Barrow, D., Matcheva, K. I., and Drossart, P., 2012. Prospects for Observing Atmospheric Gravity Waves in Jupiter's Thermosphere Using  $H_3^+$  Emission. *Icarus*, in press.
3. Conrath, B. J. and Gautier, D., 2000. Saturn Helium Abundance: A Reanalysis of Voyager Measurements. *Icarus* 144, Issue Icarus, pp. 124-134.
4. Festou, M. C., and Atreya, S. K., 1982. Voyager ultraviolet stellar occultation measurements of the composition and thermal profiles of the saturnian upper atmosphere. *Geophys. Res. Lett.* 9, 1147-1150.
5. Fischer, G., Desch, M. D., Zarka, P., Kaiser, M. L., Gurnett, D. A., Kurth, W. S., Macher, W., Rucker, H. O., Lecacheux, A., Farrell, W. M., Cecconi, B., 2006. Saturn lightning recorded by Cassini/RPWS in 2004. *Icarus* 183, Issue 1, 135-152.
6. Fischer, G. Gurnett, D. A., Zarka, P., Moore, L., Dyudina, U. A., 2011. Peak electron densities in Saturn's ionosphere derived from the low-frequency cutoff of Saturn lightning. *Journal of Geophysical Research*, Volume 116, Issue A4.
7. Fletcher, L. N., Achterberg, R. K., Greathouse, T. K., Orton, G. S., Conrath, B. J., Simon-Miller, A. A., Teanby, N., Guerlet, S., Irwin, P. G. J., Flasar, F. M., 2010. Seasonal change on Saturn from Cassini/CIRS observations, 2004-2009. *Icarus* 208, 337-352.

- 529 8. Hubbard, W. B.; Porco, C. C.; Hunten, D. M.; Rieke, G. H.; Rieke, M. J.; McCarthy,  
530 D. W.; Haemmerle, V.; Haller, J.; McLeod, B.; Lebofsky, L. A.; Marcialis, R.; Holberg,  
531 J. B.; Landau, R.; Carrasco, L.; Elias, J.; Buie, M. W.; Dunham, E. W.; Persson, S.  
532 E.; Boroson, T.; West, S.; French, R. G.; Harrington, J.; Elliot, J. L.; Forrest, W.  
533 J.; Pipher, J. L.; Stover, R. J.; Brahic, A.; Grenier, I., 1997. Structure of Saturn's  
534 Mesosphere from the 28 SGR Occultations. *Icarus* 130, 404-425.
- 535 9. Harrington, J., French, R., Matcheva, K. I., 2010. The 1998 November 14 Occultation  
536 of GSC 0622-00345 by Saturn. II. Stratospheric Thermal Profile, Power Spectrum, and  
537 Gravity Waves. *The Astrophysical Journal*, Volume 716, Issue 1, 404-416.
- 538 10. Hines, C.O., 1974. The upper atmosphere in motion. Geophysical Monograph Series,  
539 vol. 18. American Geophysical Union, Washington, DC.
- 540 11. Hinson, D. P., Flasar, M. F., Kliore, A. J., Schinder, P. J., Twicken, J. D., Herrera,  
541 R. G., 1997. Results from the first Galileo radio occultation experiment. *J. Geophys.*  
542 *Res. Lett.* 24, 2107-2110.
- 543 12. Kelley, M. C., 1989. The Earth's Ionosphere. Plasma Physics and Electrodynamics.  
544 Academic Press, San Diego, CA.
- 545 13. Kliore, A. J., Nagy, A. F., Marouf, E. A., Anabtawi, A., Barbini, E., Fleischman, D.  
546 U., Kahan, D. S., 2009. Midlatitude and high-latitude electron density profiles in the  
547 ionosphere of Saturn obtained by Cassini radio occultation observations. *Journal of*  
548 *Geophysical Research*, Volume 114, Issue A4, CiteID A04315.
- 549 14. Lindal, G. F., Sweetnam, D. N., and Eshleman, V. R., 1985. The atmosphere of Saturn:  
550 An analysis of the Voyager radio occultation measurements. *Astron. J.* 90, 1136-1146.
- 551 15. Lindzen, R.S., 1981. Turbulence and stress owing to gravity wave and tidal breakdown.  
552 *J. Geophys. Res.* 86, 9707-9714.
- 553 16. Majeed, T., McConneall, J. C., 1991. The upper ionospheres of Jupiter and Saturn.  
554 *Planetary and Space Science*, vol. 39, 1715-1732.

- 555 17. Majeed, T., McConneell, J. C., 1996. Voyager electron density measurements on Sat-  
556 urn: Analysis with a time dependent ionospheric model. *Journal of Geophysical Re-*  
557 *search*, Volume 101, Issue E3, 7589-7598.
- 558 18. Matcheva, K. I., and Strobel D. F., 1999. Heating of Jupiter's thermosphere by dis-  
559 sipation of gravity waves due to molecular viscosity and heat conduction. *Icarus* 140,  
560 328-340.
- 561 19. Matcheva, K. I., Strobel, D. F., Flasar, F. M., 2001. Interaction of gravity waves with  
562 ionospheric plasma: Implications for Jupiter's ionosphere. *Icarus* 152, 347-365.
- 563 20. Melin, H., Stallard, T., Miller, S., Gustin, J., Galand, M., Badman S., Pryor, W.,  
564 O'Donoghue, J., Brown, R., and K. H. Baines, 2011. Simultaneous Cassini VIMS and  
565 UVIS observations of Saturn's southern aurora: Comparing emissions from H,  $H_2$  and  
566  $H_3^+$  at a high spatial resolution. *Geophys. Res. Lett.*, 38, L15203, doi:10.1029/2011GL048457.
- 567 21. Moses, J. I. and Bass, S. F., 2000. The effects of external material on the chemistry  
568 and structure of Saturn's ionosphere. *Journal of Geophysical Research*, Volume 105,  
569 Issue E3, 7013-7052.
- 570 22. Moses, J. I., Bezard, B., Lellouch, E., Gladstone, G., Feuchtgruber, H., Allen, M., 2000,  
571 Photochemistry of Saturn's Atmosphere: I. Hydrocarbon Chemistry and Comparison  
572 with ISO Observations. *Icarus* 143, 244-298.
- 573 23. Moore, L. E., Mendillo, M., Mueller-Wodarg, I. C. F., Murr, D. L., 2004. Modeling of  
574 global variations and ring shadowing in Saturn's ionosphere. *Icarus* 172, 503-520.
- 575 24. Moore, L., Mueller-Wodarg, I., Galand, M., Kliore, A., Mendillo, M., 2010. Latitudi-  
576 nal variations in Saturn's ionosphere: Cassini measurements and model comparisons.  
577 *Journal of Geophysical Research*, Volume 115, Issue A11, CiteID A11317.
- 578 25. Nagy, A. F., Kliore, A. J., Marouf, E., French, R., Flasar, M., Rappaport, N. J.,  
579 Anabtawi, A., Asmar, S. W., Johnston, D., Barbini, E., Goltz, G., Fleischman, D.,  
580 2006. First results from the ionospheric radio occultations of Saturn by the Cassini  
581 spacecraft. *Journal of Geophysical Research*, Volume 111, Issue A6, CiteID A06310.

- 582 26. Nagy, A. , Arvydas J. Kliore, Michael Mendillo, Steve Miller, Luke Moore, Julianne  
583 I. Moses, Ingo Mueller-Wodarg, and Don Shemansky, 2009. Upper Atmosphere and  
584 Ionosphere of Saturn. in "Saturn from Cassini-Huygens", by Dougherty, Michele K.;  
585 Esposito, Larry W.; Krimigis, Stamatios M., ISBN 978-1-4020-9216-9. Springer Science  
586 Business Media B.V., p. 181.
- 587 27. Smith, G. R., Shemansky, D. E., Holberg, J. B., Broadfoot, A. L., Sandel, B. R., and  
588 McConnell, J. C., 1983. Saturn's upper atmosphere from the Voyager 2 EUV solar and  
589 stellar occultations. *J. Geophys. Res.* 88, 8667-8678.
- 590 28. Torrence, C. and Compo, P., 1998. A practical Guide to Wavelet Analysis. *Bull.*  
591 *Amer. Meteor. Soc.*, 79, 61-78.
- 592 29. Walterscheid, R.L., 1981. Dynamical cooling induced by dissipating internal gravity  
593 waves. *J. Geophys. Res. Lett.* 8, 1235-1238.
- 594 30. Warwick, J. W., Evans, D. R., Romig, J. H., Alexander, J. K., Desch, M. D., Kaiser,  
595 M. L., Aubier, M. G., Leblanc, Y., Lecacheux, A., Pedersen, B. M., 1982. Planetary  
596 radio astronomy observations from Voyager 2 near Saturn. *Science*, vol. 215, Jan. 29,  
597 1982, p. 582-587.
- 598 31. Warwick, J. W., Pearce, J. B., Evans, D. R., Carr, T. D., Schauble, J. J., Alexander,  
599 J. K., Kaiser, M. L., Desch, M. D., Pedersen, M., Lecacheux, A., Daigne, G., Boischot,  
600 A., Barrow, C. H., 1981. Planetary radio astronomy observations from Voyager 1 near  
601 Saturn. *Science*, vol. 212, Apr. 10, 1981, p. 239-243.

602 **List of Tables:**

603 **Table I:** Summary of the vertical scales of variability identified in the electron density  
604 profiles shown in Figs. 1-4.

ACCEPTED MANUSCRIPT

TABLE I

Latitude	Obs.	Dawn/Dusk	$S$ [km]	$Z_{max}$	$\Delta N_{e,max}$ [ $\text{cm}^{-3}$ ]
72°S	S56 exit	dusk	500	700-1800 km	1000
			250	1000	2500
			165	1200	2000
28°S	S68 entry	dusk	430	1350	5000
			210	1000	2000
3°S	S08 entry	dusk	380	1250	2000
9°S	S07 exit	dawn	570	800	190
			360	1800	150

Table I: Summary of the vertical scales of variability ( $S < 700$  km) identified in the electron density profiles shown in Figs. 1-4.

606 List of Figures and figure captions:

607

608 **Figure 1:** High latitude dusk observation (72°S). Left panel: Electron density profile  
 609 from S56 exit radio occultation. Central panel: Electron density variations as a function  
 610 of scale and altitude. Right panel: Amplitude of the variations as a function of scale and  
 611 altitude. Contours (solid black lines) are drawn at 5% increments. In the right panel the  
 612 light solid lines mark the height of dissipation,  $z_d$ , for gravity waves with a period 30 min  
 613 (line A) and 10 hours (line B). Throughout the paper altitude is measured with respect to  
 614 the 1 bar pressure level.

615

616 **Figure 2:** As in Fig. 1, but for the mid-latitude dusk observation at 28°S from the S68  
 617 entry radio occultation.

618

619 **Figure 3:** As in Fig. 1, but for the low latitude dusk observation at 3°S from the S08  
 620 entry radio occultation.

621

622 **Figure 4:** As in Fig. 1, but for the low latitude dawn observation at 9°S from the S07  
 623 exit radio occultation.

624

625 **Figure 5:** Wavelet analysis for S56 exit occultation (see Fig. 1) together with the 5%  
 626 significance level contour (black solid line) as defined by Torrence and Compo (1998). All  
 627 identifiable scales are well above the 5% significance level.

628

629 **Figure 6:** Histogram of the number of detections of individual scales with an amplitude  
 630 larger than 5%. The count is normalized by the corresponding number of observations: a) all  
 631 electron density profiles (31 observations); b) high latitudes only (8 observations); c) middle  
 632 latitudes (7 observations); d) low latitudes (16 observations).

633

634 **Figure 7:** As in Fig. 6, but for: a) low latitude dawn conditions (8 observations); b) low  
 635 latitude dusk conditions (8 observations).

636

637 **Figure 8:** As in Fig. 6, but for: a) all altitudes observations during 2005 (12 observa-  
638 tions); b) all altitudes observations during 2007-2008 (14 observations).

639

640 **Figure 9:** Structure of the steady state neutral atmosphere.

641

642 **Figure 10:** Atmospheric gravity wave model. Bottom axis: wave amplitude profile (red  
643 - vertical velocity; green - horizontal velocity; blue - temperature profile). Top axis: vertical  
644 wavelength in black solid line.

645

646 **Figure 11:** Wave dissipation altitude. Each curve corresponds to a family of waves  
647 with the same period ranging from 30 min (top curve) period to 10 hours (bottom curve) in  
648 increments of 10 min.

649

## 650 APPENDIX

651

652 **Figure A.1** As in Fig. 1, but for the low latitude dusk observation at  $4.9^{\circ}\text{S}$  from S07  
653 entry radio occultation.

654

655 **Figure A.2:** As in Fig. 1, but for the low latitude dawn observation at  $8.3^{\circ}\text{S}$  from S08  
656 exit radio occultation.

657

658 **Figure A.3:** As in Fig. 1, but for the low latitude dawn observation at  $7.4^{\circ}\text{S}$  from S09  
659 exit radio occultation. Note that contours (solid black lines) are drawn at 10% increments  
660 starting at 5%.

661

662 **Figure A.4:** As in Fig. 1, but for the low latitude dusk observation at  $1.6^{\circ}\text{N}$  from S10  
663 entry radio occultation.

664

665 **Figure A.5:** As in Fig. 1, but for the low latitude dawn observation at  $6.1^{\circ}\text{S}$  from S10  
666 exit radio occultation.

667

668 **Figure A.6:** As in Fig. 1, but for the low latitude dawn observation at  $4.5^{\circ}\text{S}$  from S11  
669 exit radio occultation.

670

671 **Figure A.7:** As in Fig. 1, but for the low latitude dusk observation at  $7.5^{\circ}\text{N}$  from S12  
672 entry radio occultation.

673

674 **Figure A.8:** As in Fig. 1, but for the low latitude dawn observation at  $2.6^{\circ}\text{S}$  from S12  
675 exit radio occultation.

676

677 **Figure A.9:** As in Fig. 1, but for the low latitude dawn observation at  $0.5^{\circ}\text{S}$  from S13  
678 exit radio occultation.

679

680 **Figure A.10:** As in Fig. 1, but for the low latitude dusk observation at  $8.4^{\circ}\text{S}$  from S14  
681 entry radio occultation.

682

683 **Figure A.11:** As in Fig. 1, but for the low latitude dusk observation at  $5.0^{\circ}\text{S}$  from S28  
684 entry radio occultation.

685

686 **Figure A.12:** As in Fig. 1, but for the high latitude observation at  $75.4^{\circ}\text{N}$  from S44  
687 entry radio occultation.

688

689 **Figure A.13:** As in Fig. 1, but for the low latitude dawn observation at  $3.2^{\circ}\text{S}$  from S44  
690 exit radio occultation.

691

692 **Figure A.14:** As in Fig. 1, but for the low latitude dusk observation at  $5.0^{\circ}\text{S}$  from S46  
693 exit radio occultation.

694

695 **Figure A.15:** As in Fig. 1, but for the middle latitude dawn observation at  $41.2^{\circ}\text{N}$  from  
696 S47 exit radio occultation.

697

698 **Figure A.16:** As in Fig. 1, but for the middle latitude dusk observation at  $38.7^{\circ}\text{S}$  from  
699 S51 entry radio occultation.

700

701 **Figure A.17:** As in Fig. 1, but for the middle latitude dawn observation at  $43.6^{\circ}\text{S}$  from  
702 S51 exit radio occultation.

703

704 **Figure A.18:** As in Fig. 1, but for the low latitude dusk observation at  $17.9^{\circ}\text{S}$  from S54  
705 entry radio occultation.

706

707 **Figure A.19:** As in Figure 1, but for the high latitude observation at  $68.7^{\circ}\text{S}$  from S54  
708 exit radio occultation.

709

710 **Figure A.20:** As in Figure 1, but for the high latitude observation at  $74.1^{\circ}\text{S}$  from S58  
711 exit radio occultation.

712

713 **Figure A.21:** As in Figure 1, but for the high latitude observation at  $65.6^{\circ}\text{S}$  from S68  
714 exit radio occultation.

715

716 **Figure A.22:** As in Fig. 1, but for the middle latitude dusk observation at  $42.3^{\circ}\text{S}$  from  
717 S70 entry radio occultation.

718

719 **Figure A.23:** As in Fig. 1, but for the high latitude observation at  $69.1^{\circ}\text{S}$  from S70 exit  
720 radio occultation.

721

722 **Figure A.24:** As in Fig. 1, but for the middle latitude dusk observation  $40.5^{\circ}\text{N}$  from  
723 S72 entry radio occultation.

724

725 **Figure A.25:** As in Fig. 1, but for the high latitude observation at  $66.1^{\circ}\text{S}$  from S72 exit  
726 radio occultation.

727

728 **Figure A.26:** As in Fig. 1, but for the middle latitude dusk observation at  $34.2^{\circ}\text{N}$  from  
729 S75 entry radio occultation.

730

731 **Figure A.27:** As in Fig. 1, but for the high latitude observation at  $61.8^{\circ}\text{S}$  from S75 exit  
732 radio occultation.

733

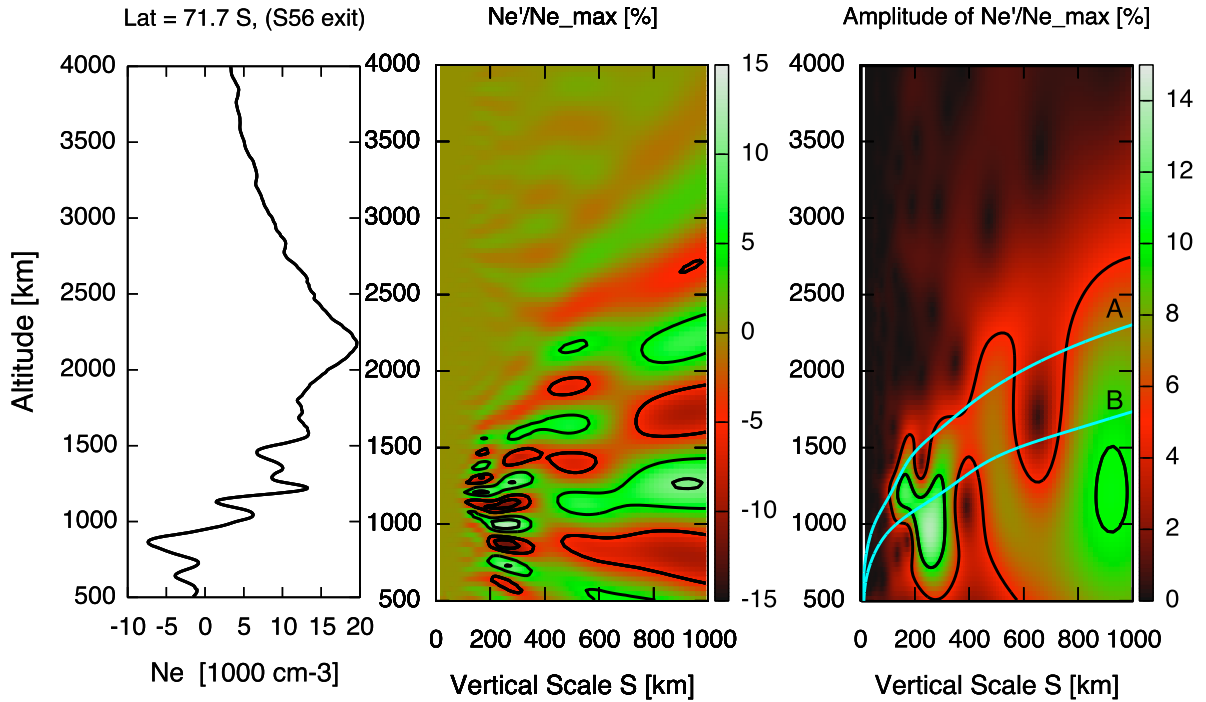


Figure 1: High latitude dusk observation ( $72^{\circ}\text{S}$ ). Left panel: Electron density profile from S56 exit radio occultation. Central panel: Electron density variations as a function of scale and altitude. Right panel: Amplitude of the variations as a function of scale and altitude. Contours (solid black lines) are drawn at 5% increments. In the right panel the light solid lines mark the height of dissipation,  $z_d$ , for gravity waves with a period 30 min (line A) and 10 hours (line B). Throughout the paper altitude is measured with respect to the 1 bar pressure level.

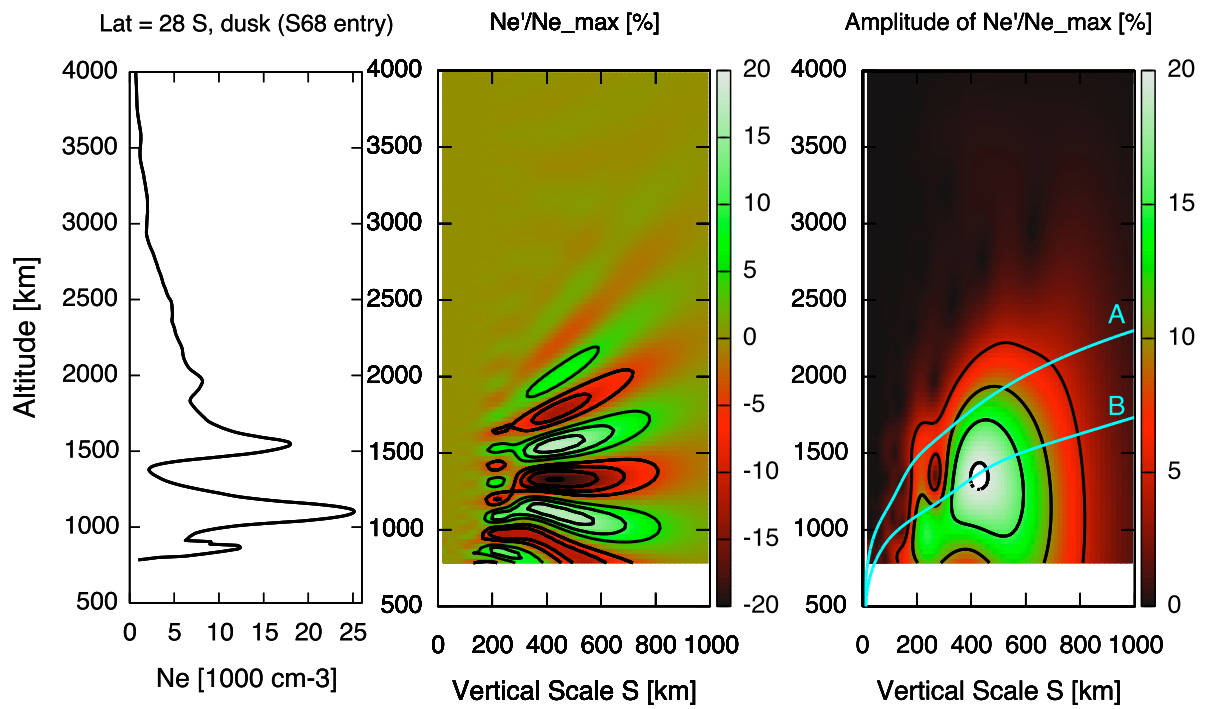


Figure 2: As in Fig. 1, but for the mid-latitude dusk observation at 28°S from the S68 entry radio occultation.

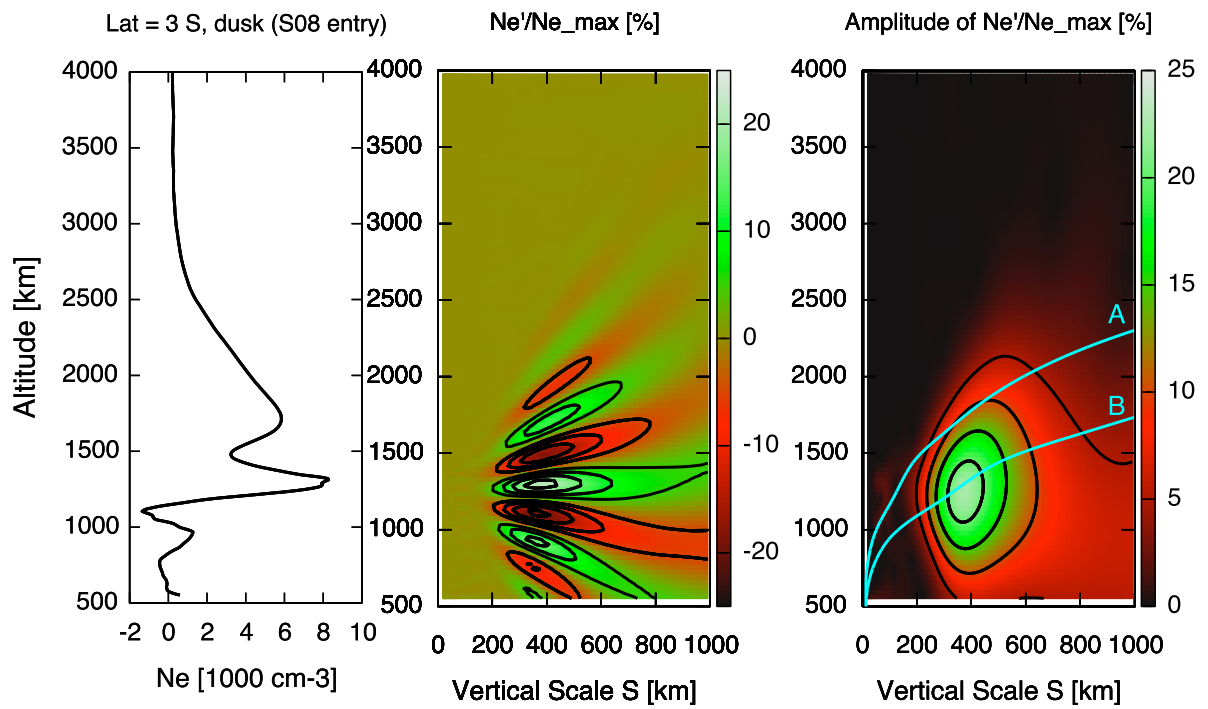


Figure 3: As in Fig. 1, but for the low latitude dusk observation at  $3^\circ\text{S}$  from the S08 entry radio occultation.

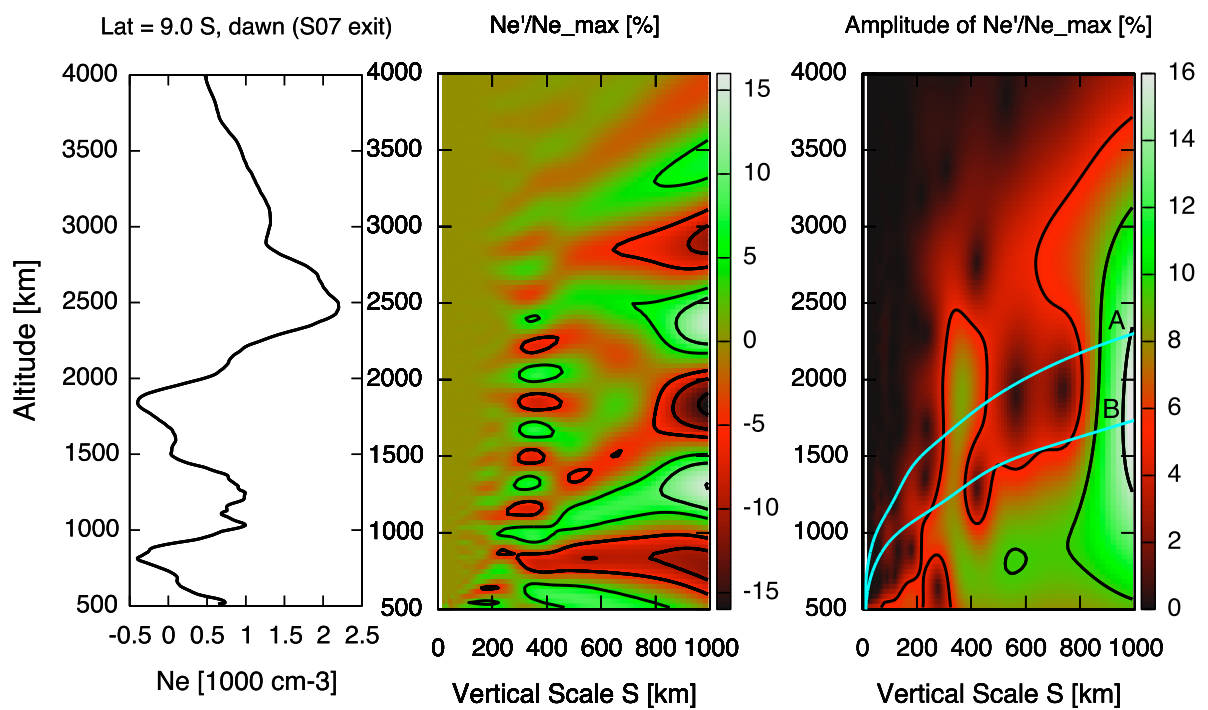


Figure 4: As in Fig. 1, but for the low latitude dawn observation at 9°S from the S07 exit radio occultation.

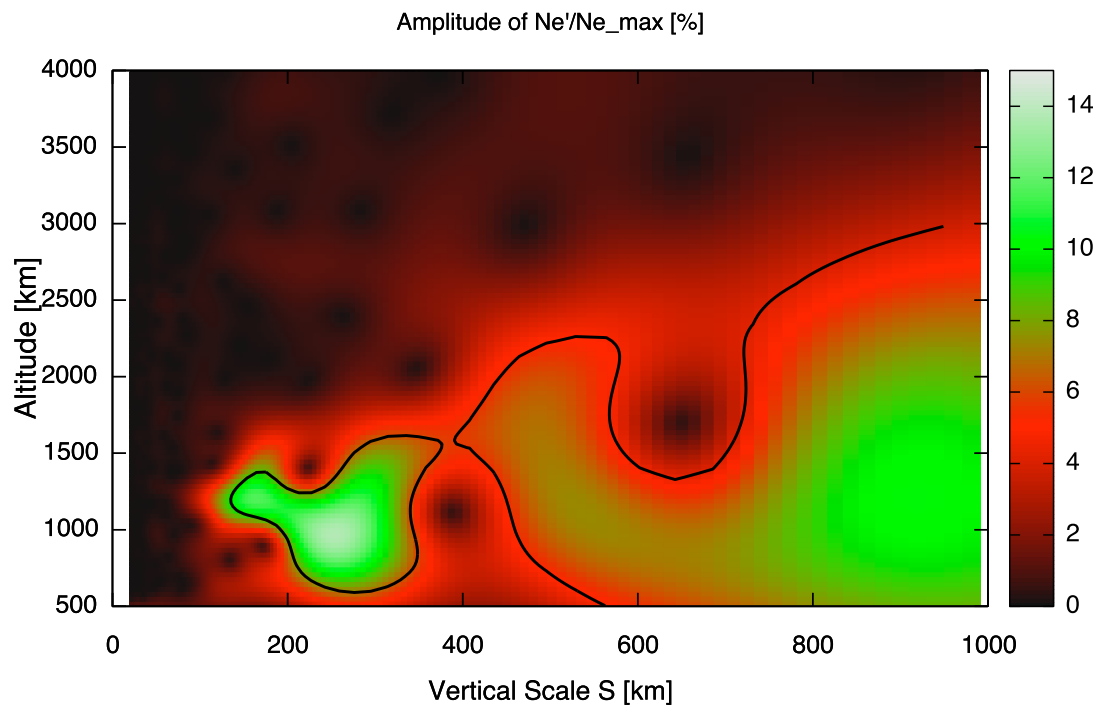


Figure 5: Wavelet analysis for S56 exit occultation (see Fig. 1) together with the 5% significance level contour (black solid line) as defined by Torrence and Compo (1998). All identifiable scales are well above the 5% significance level.

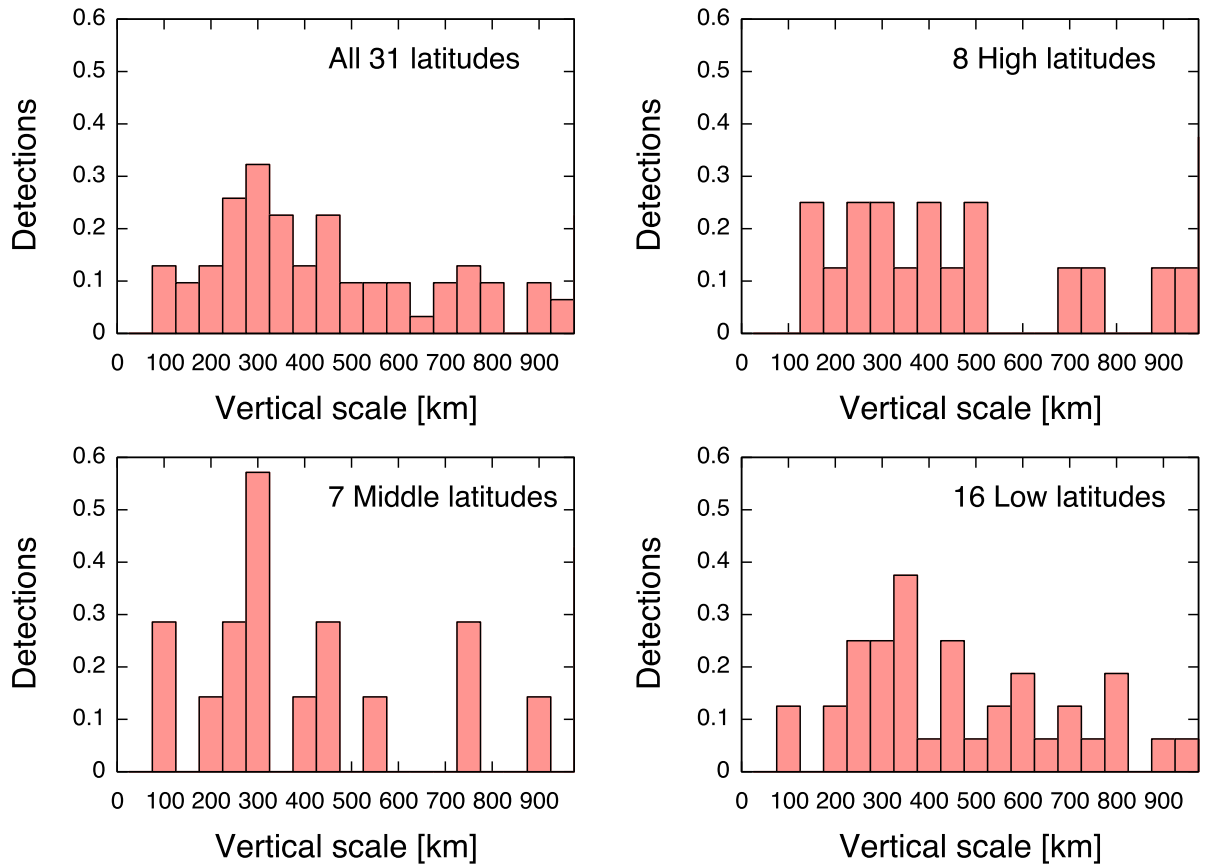


Figure 6: Histogram of the number of detections of individual scales with an amplitude larger than 5%. The count is normalized by the corresponding number of observations: a) all electron density profiles (31 observations); b) high latitudes only (8 observations); c) middle latitudes (7 observations); d) low latitudes (16 observations).

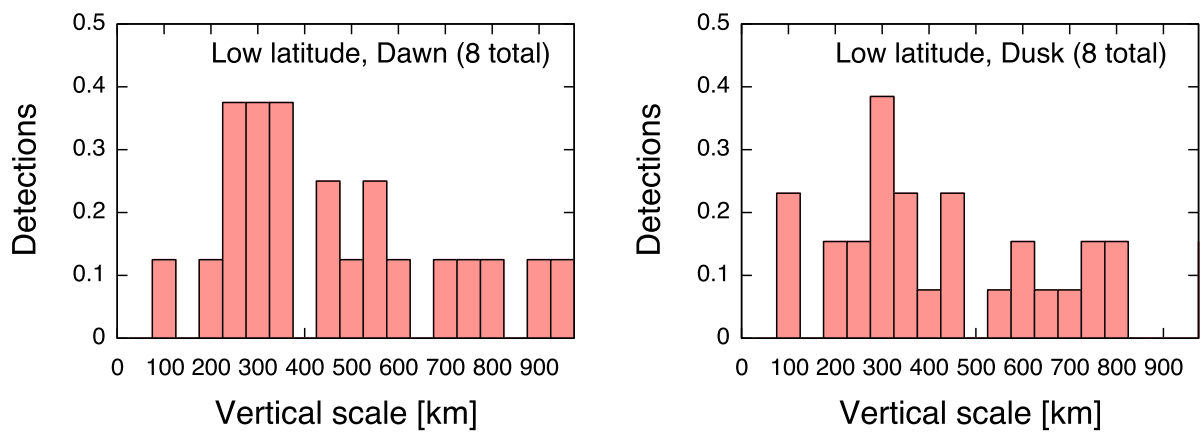


Figure 7: As in Fig. 6, but for: a) low latitude dawn conditions (8 observations); b) low latitude dusk conditions (8 observations).

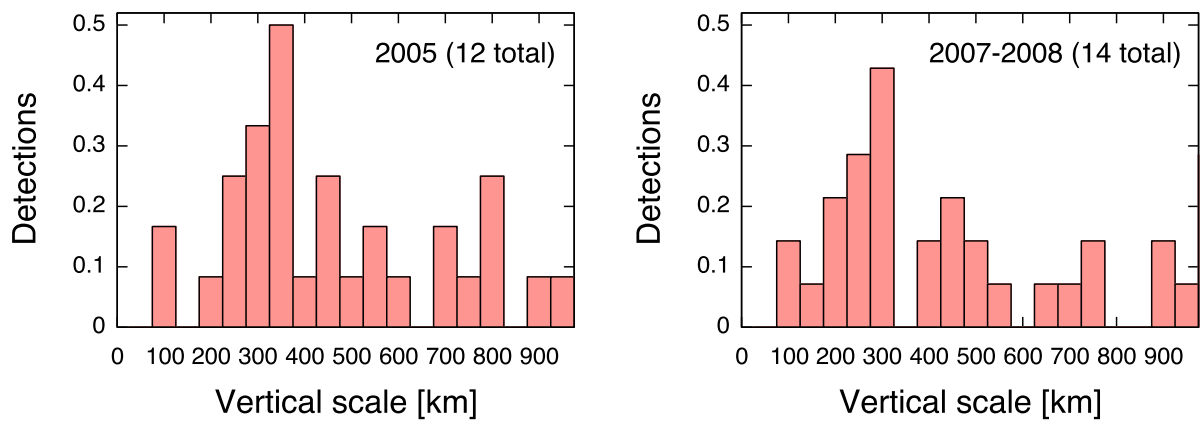


Figure 8: As in Fig. 6, but for: a) all altitudes observations during 2005 (12 observations); b) all altitudes observations during 2007-2008 (14 observations).

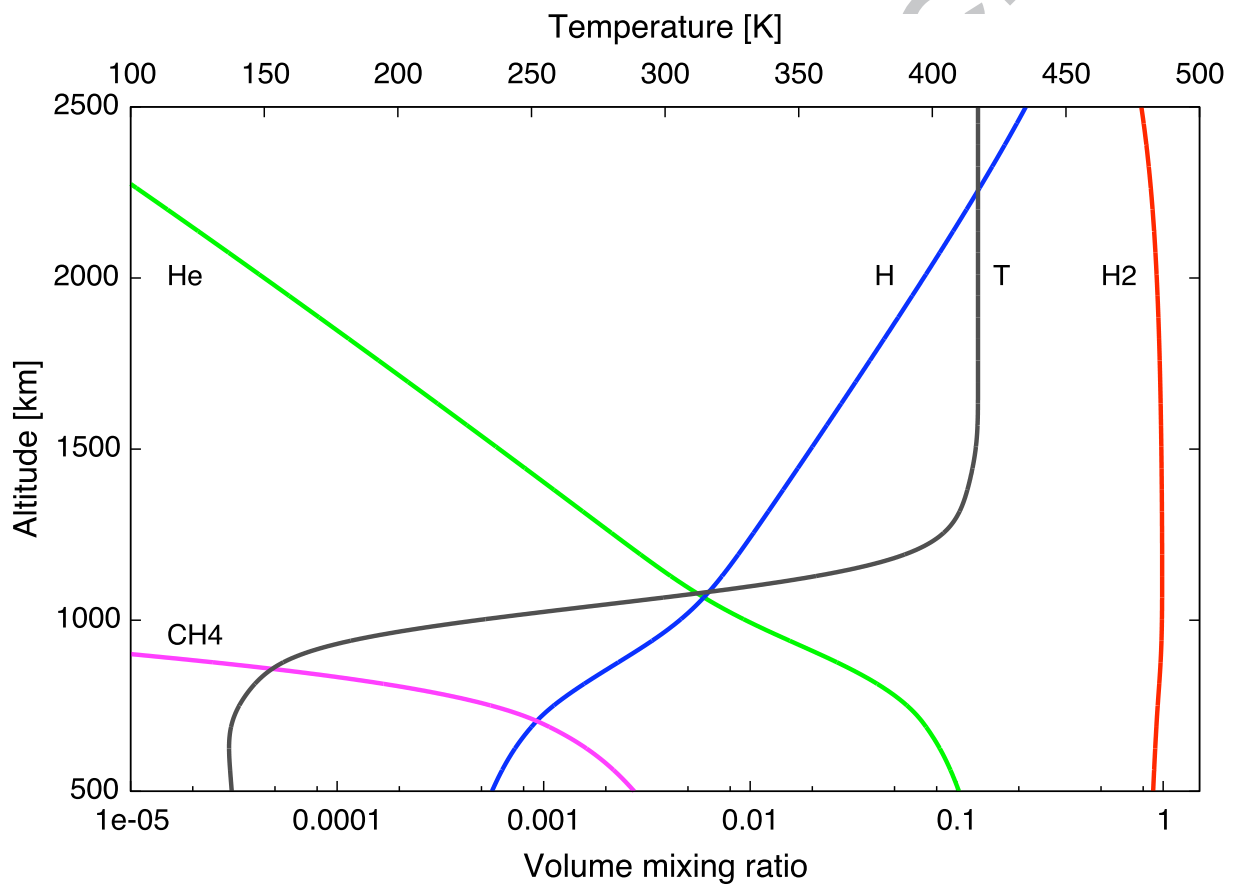


Figure 9: Structure of the steady state neutral atmosphere.

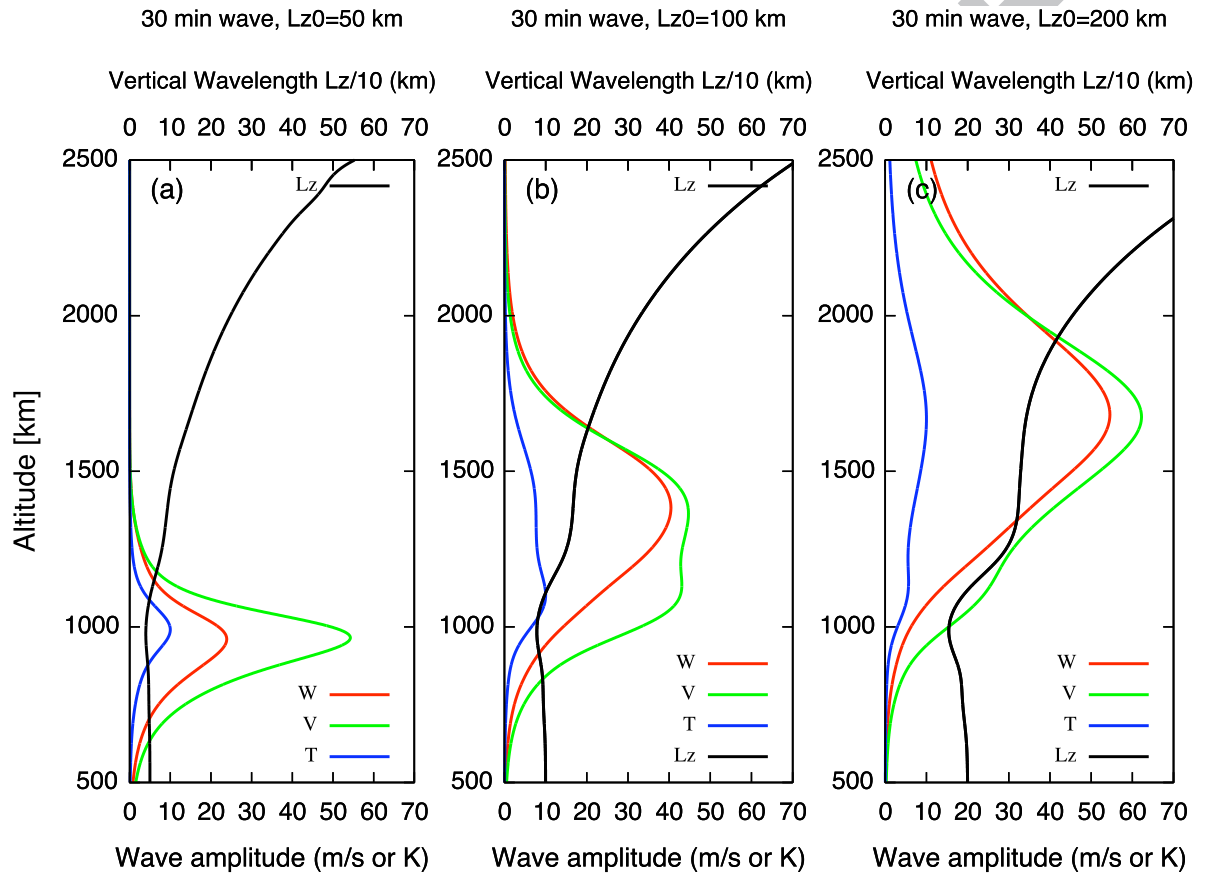


Figure 10: Atmospheric gravity wave model. Bottom axis: wave amplitude profile (red - vertical velocity; green - horizontal velocity; blue - temperature profile). Top axis: vertical wavelength in black solid line.

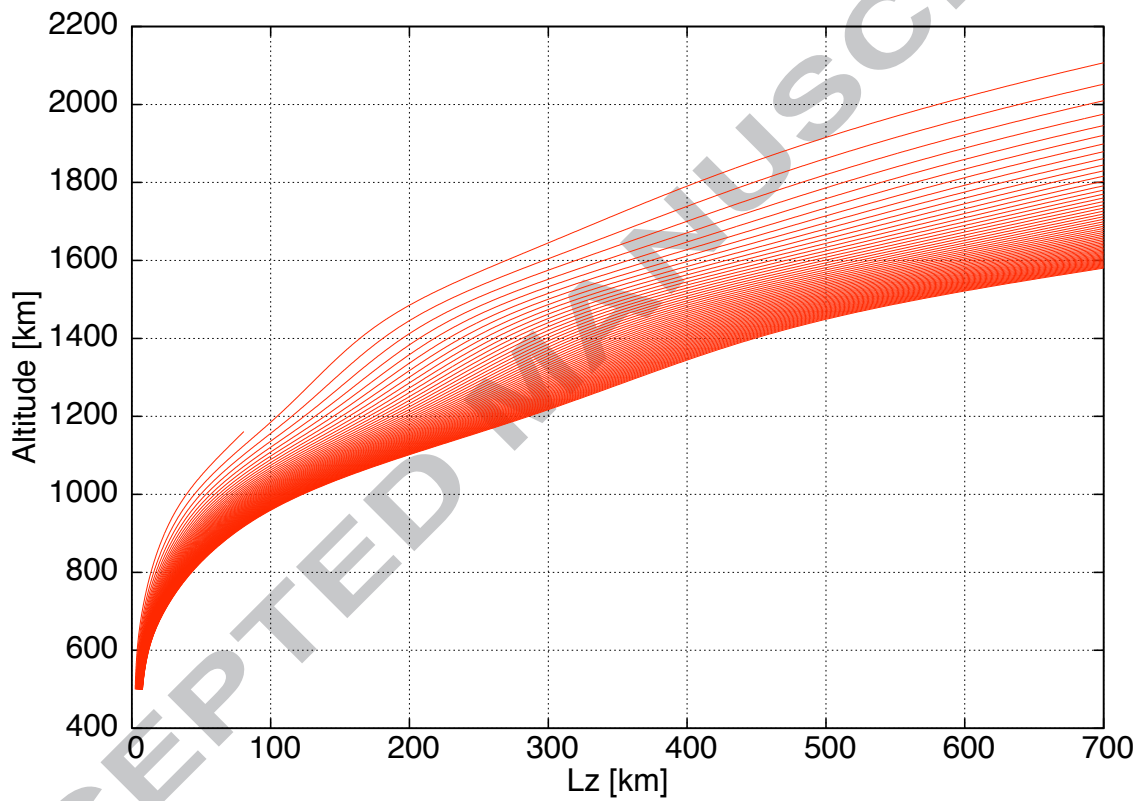


Figure 11: Wave dissipation altitude. Each curve corresponds to a family of waves with the same period ranging from 30 min (top curve) period to 10 hours (bottom curve) in increments of 10 min.

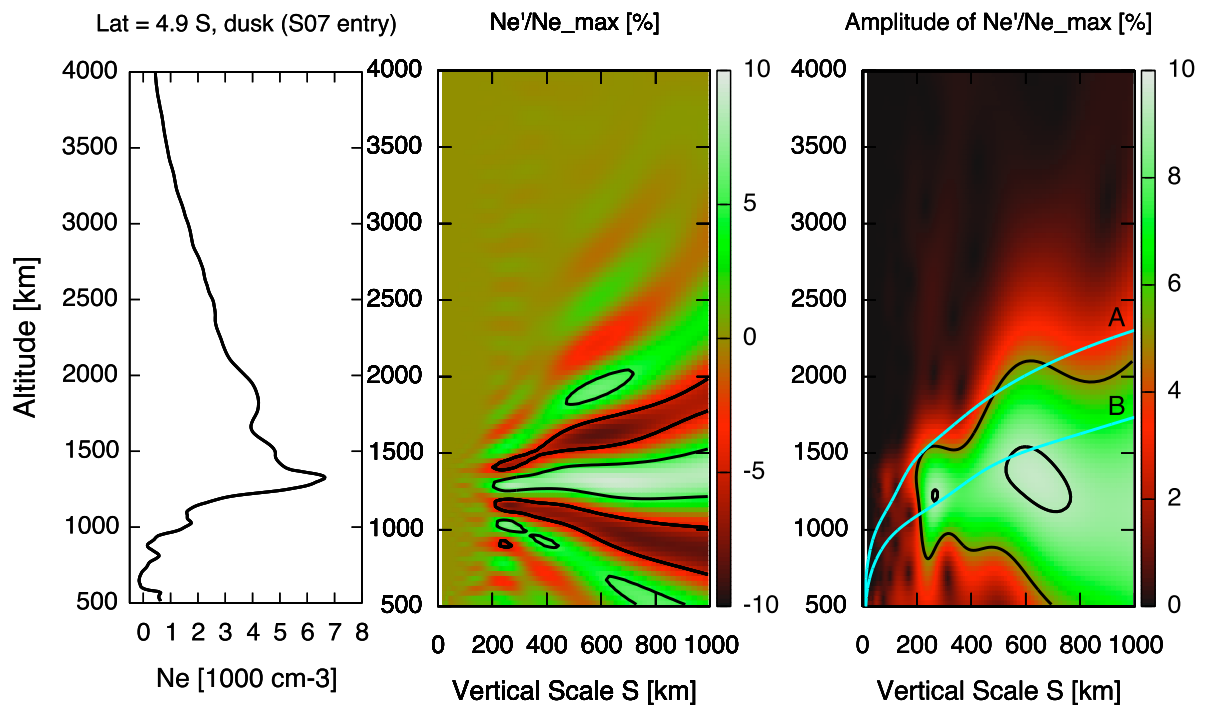


Figure A.1: As in Fig. 1, but for the low latitude dusk observation at 4.9°S from S07 entry radio occultation.

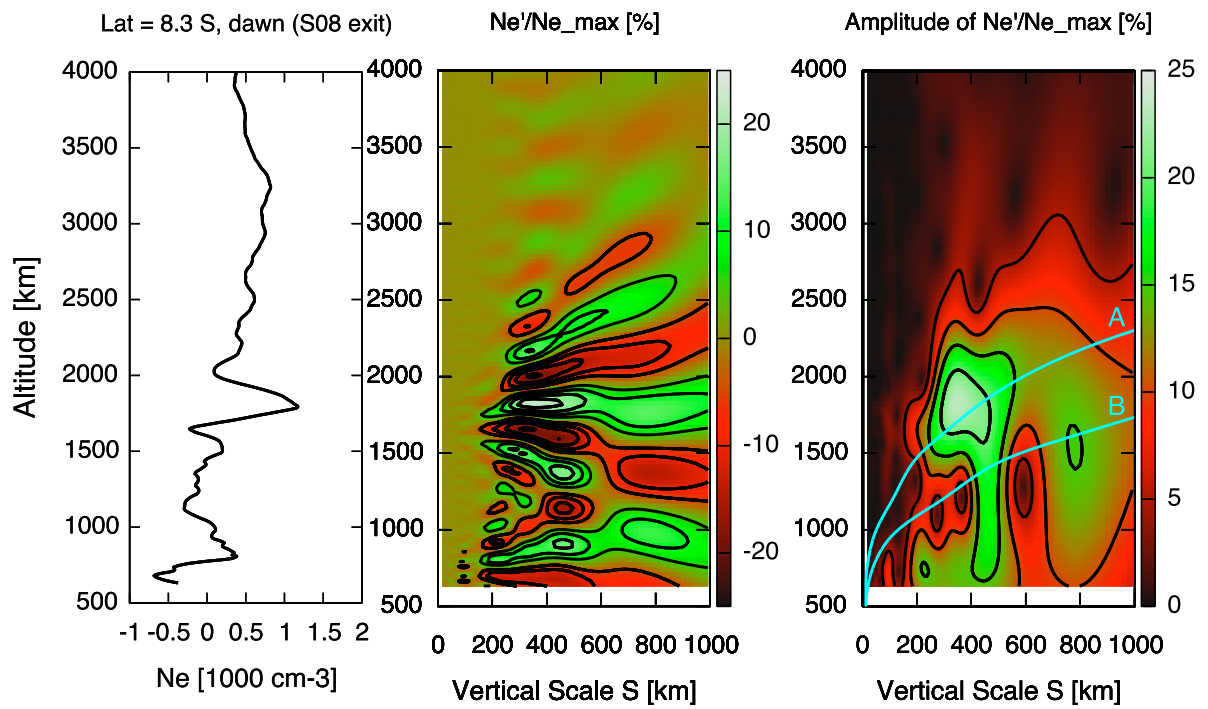


Figure A.2: As in Fig. 1, but for the low latitude dawn observation at 8.3°S from S08 exit radio occultation.

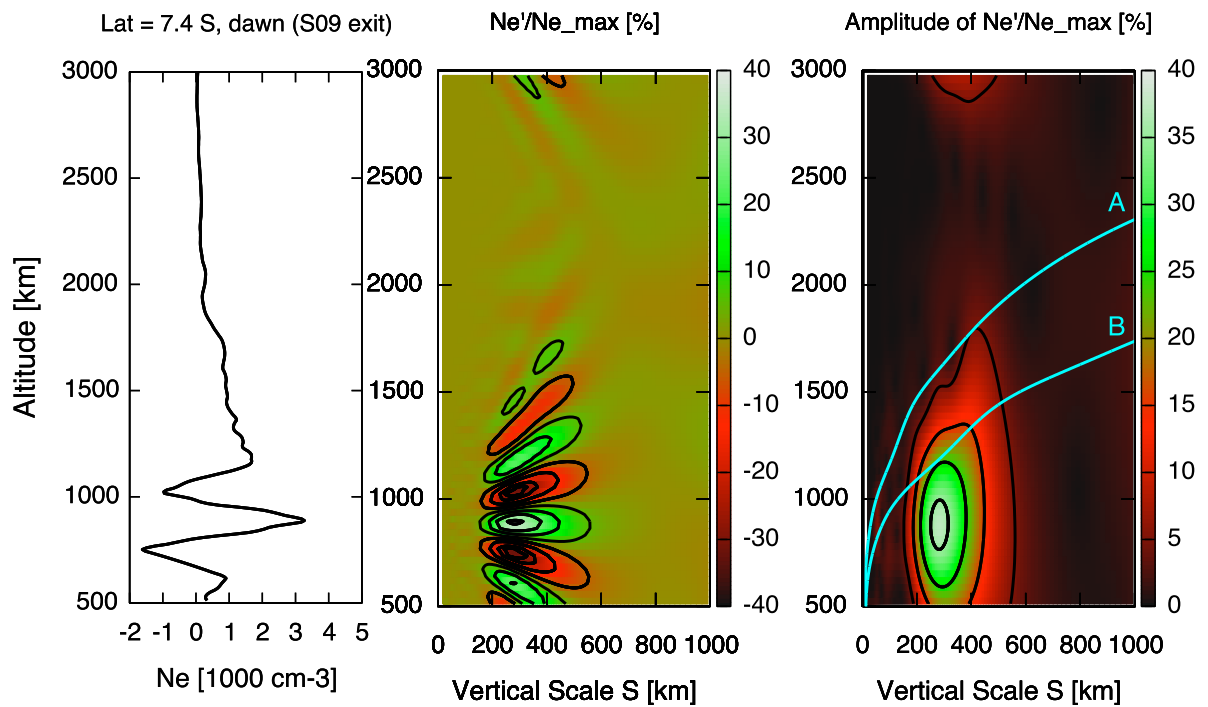


Figure A.3: As in Fig. 1, but for the low latitude dawn observation at 7.4°S from S09 exit radio occultation. Note that contours (solid black lines) are drawn at 10% increments starting at 5%.

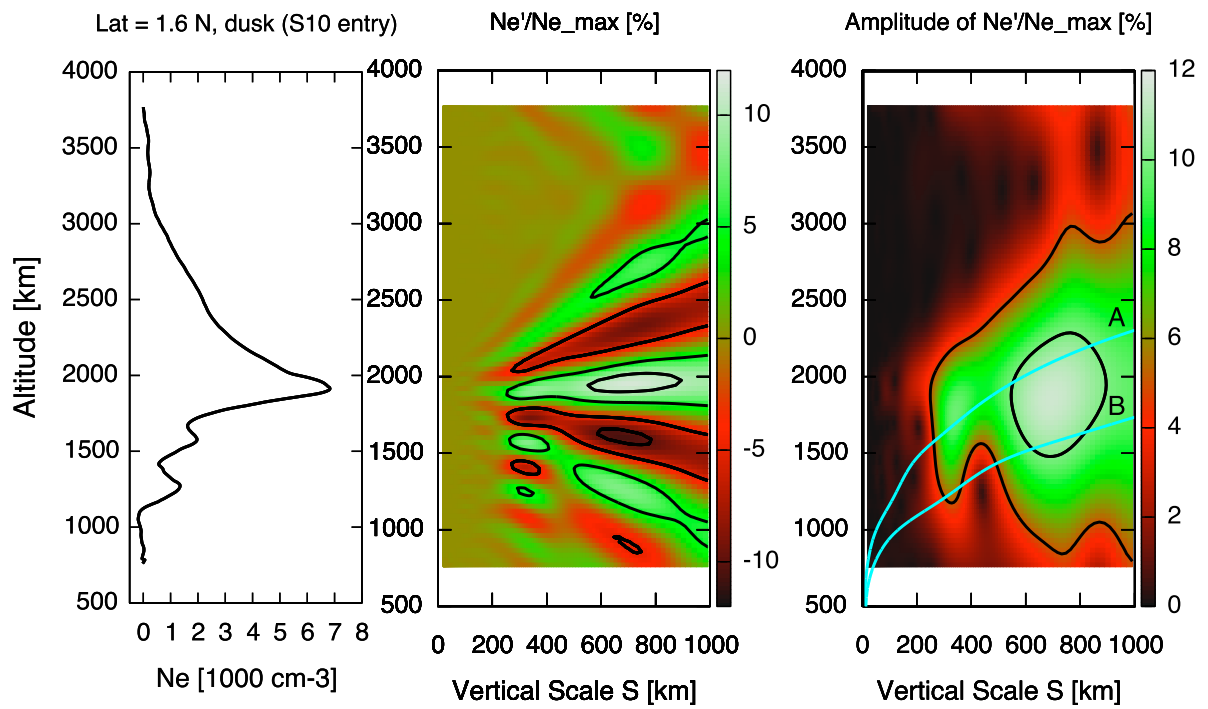


Figure A.4: As in Fig. 1, but for the low latitude dusk observation at 1.6°N from S10 entry radio occultation.

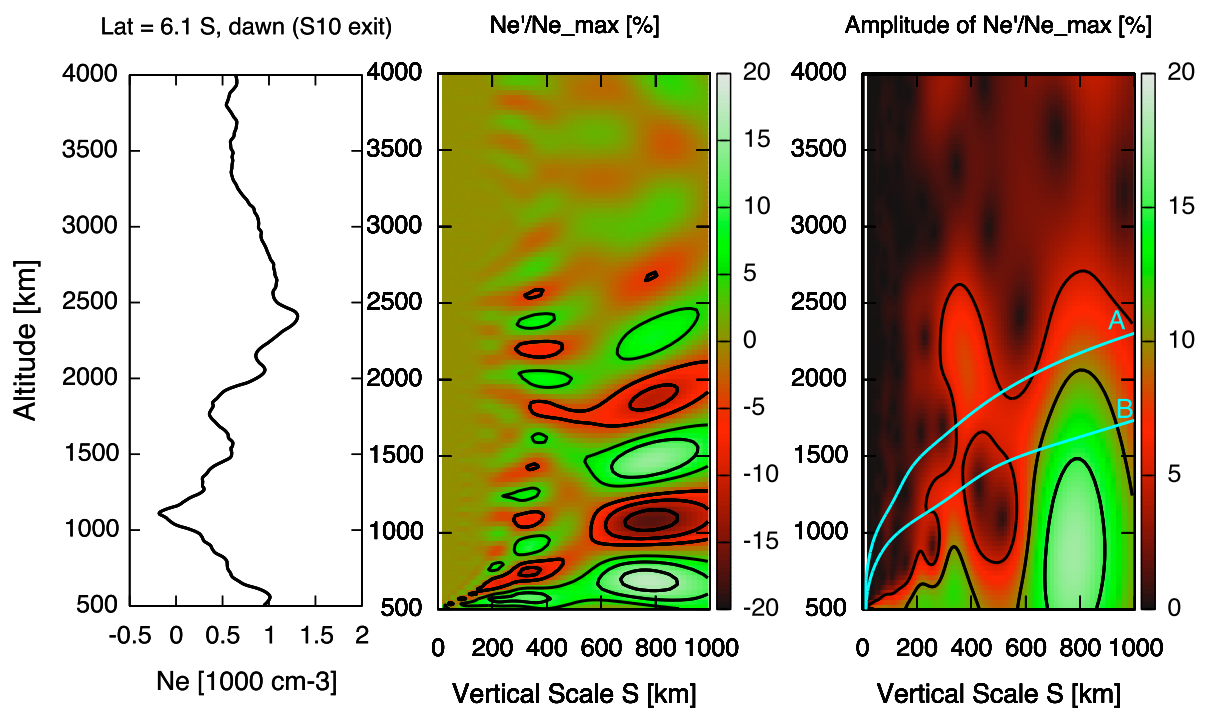


Figure A.5: As in Fig. 1, but for the low latitude dawn observation at  $6.1^\circ\text{S}$  from S10 exit radio occultation.

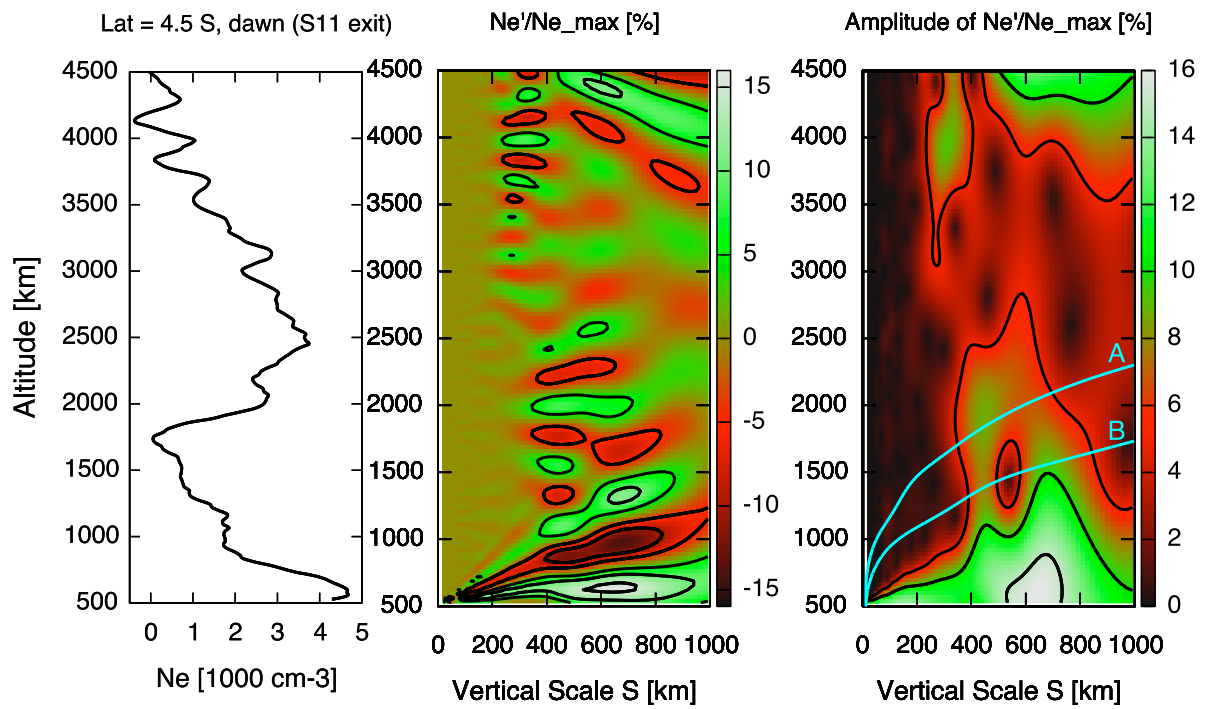


Figure A.6: As in Fig. 1, but for the low latitude dawn observation at  $4.5^\circ\text{S}$  from S11 exit radio occultation.

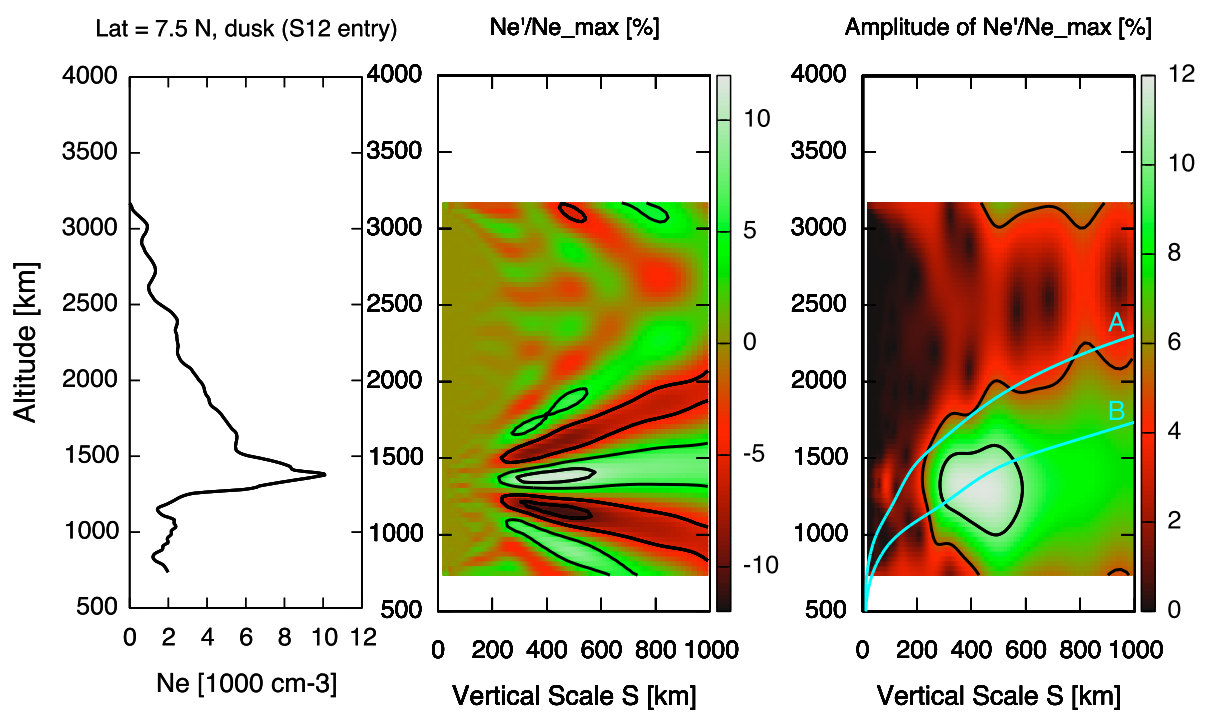


Figure A.7: As in Fig. 1, but for the low latitude dusk observation at 7.5°N from S12 entry radio occultation.

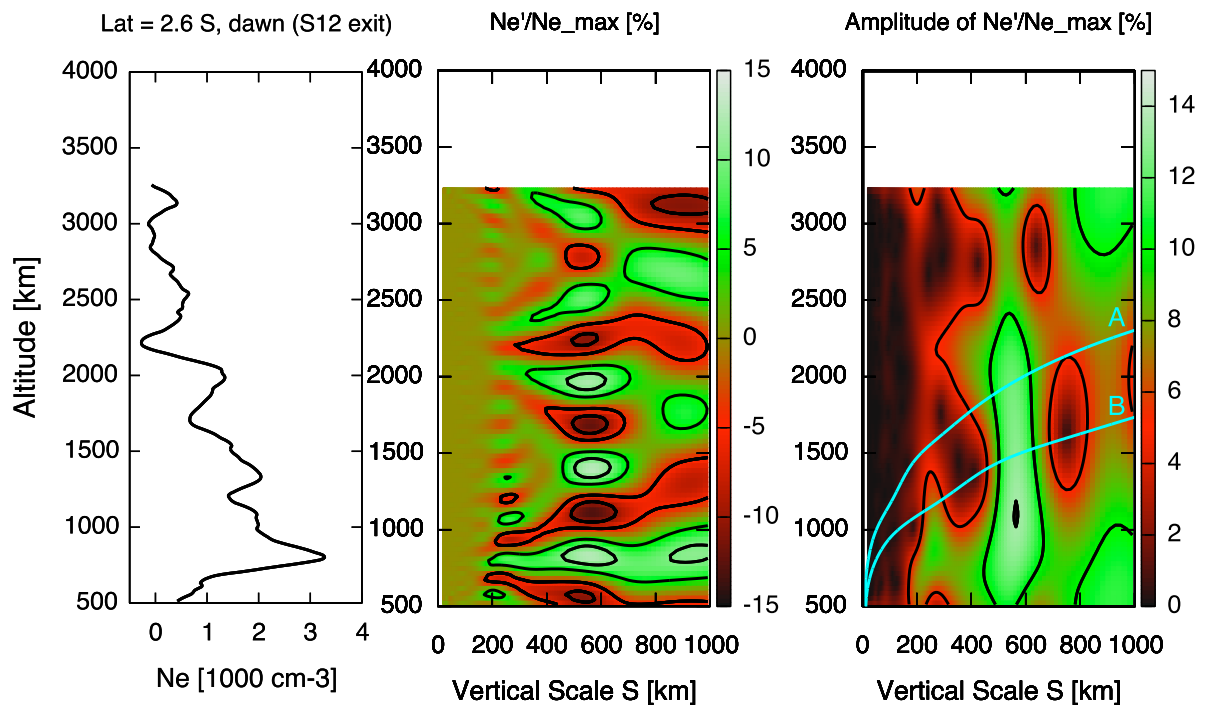


Figure A.8: As in Fig. 1, but for the low latitude dawn observation at 2.6°S from S12 exit radio occultation.

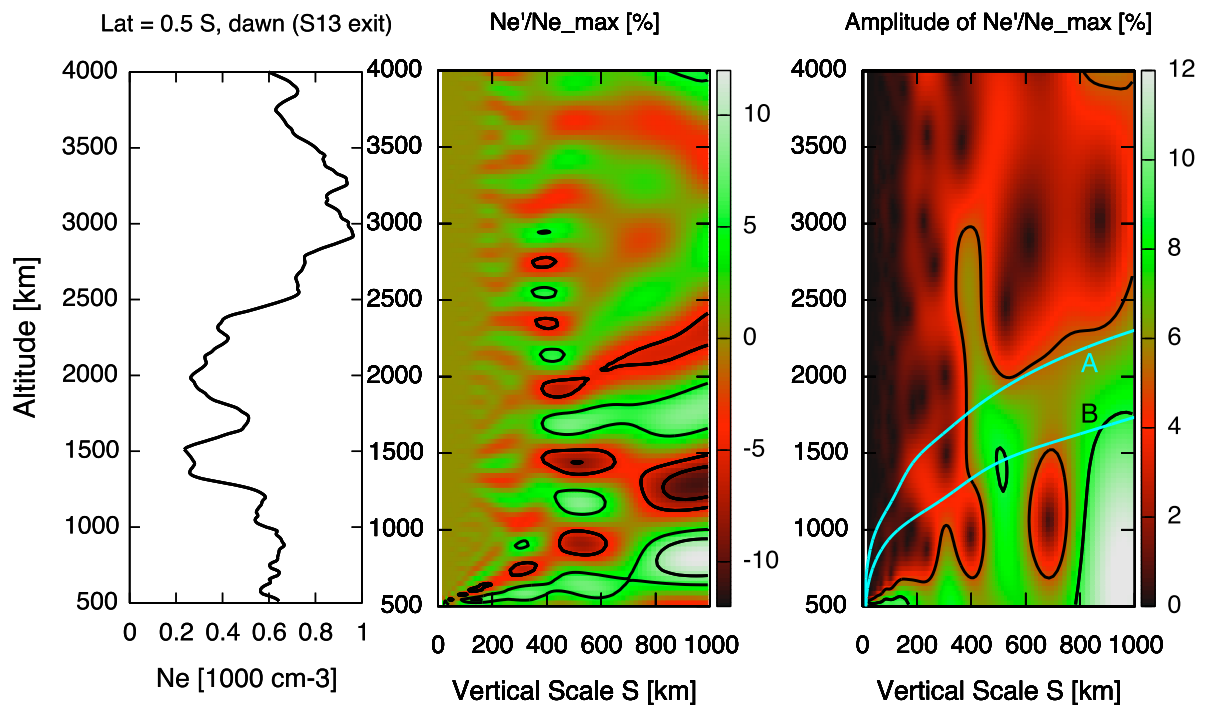


Figure A.9: As in Fig. 1, but for the low latitude dawn observation at 0.5°S from S13 exit radio occultation.

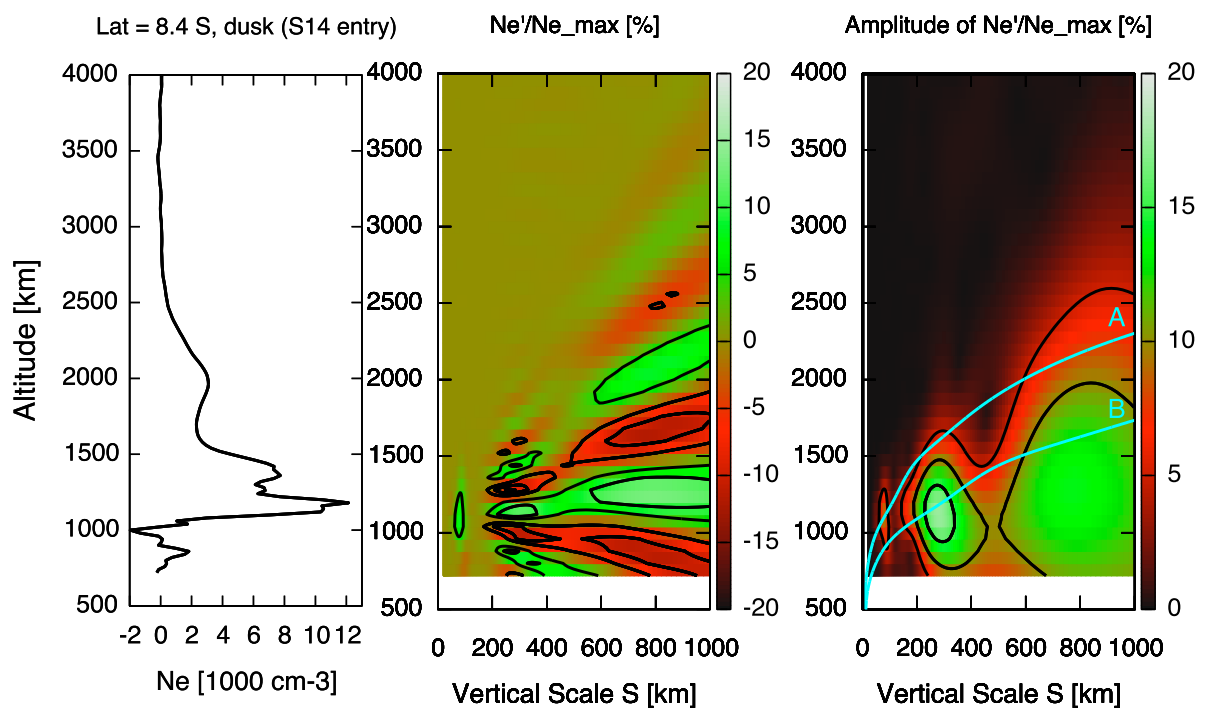


Figure A.10: As in Fig. 1, but for the low latitude dusk observation at  $8.4^\circ\text{S}$  from S14 entry radio occultation.

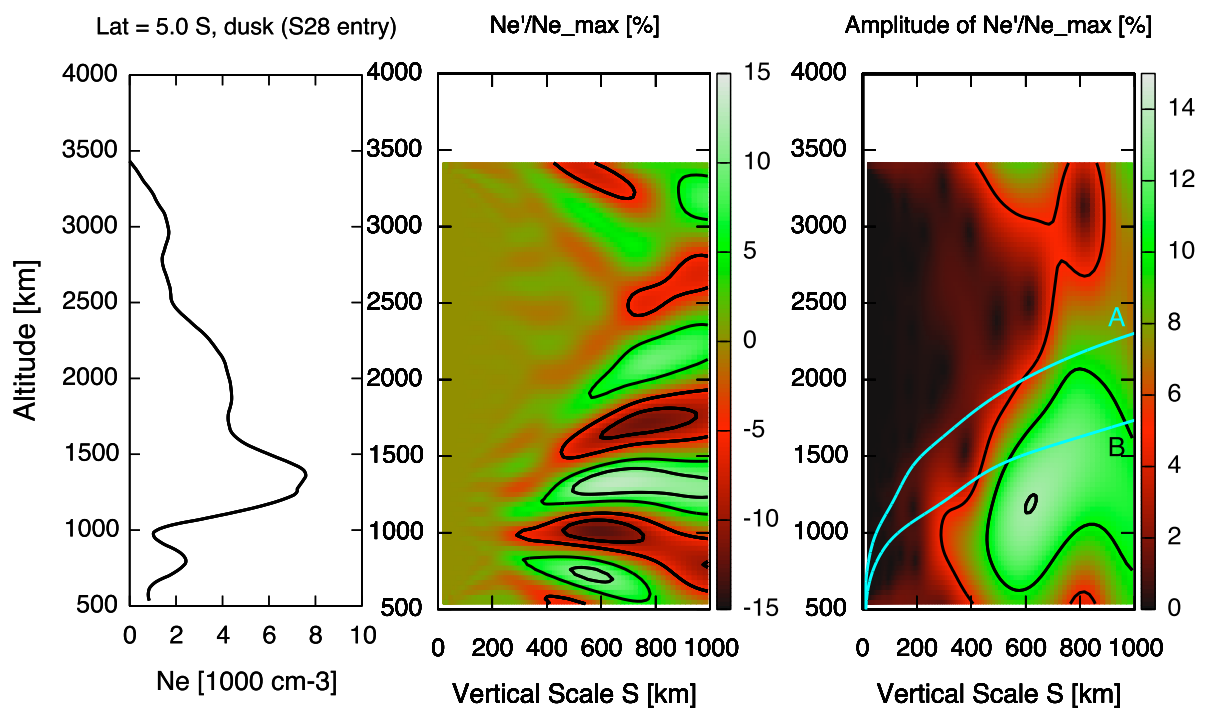


Figure A.11: As in Fig. 1, but for the low latitude dusk observation at 5.0°S from S28 entry radio occultation.

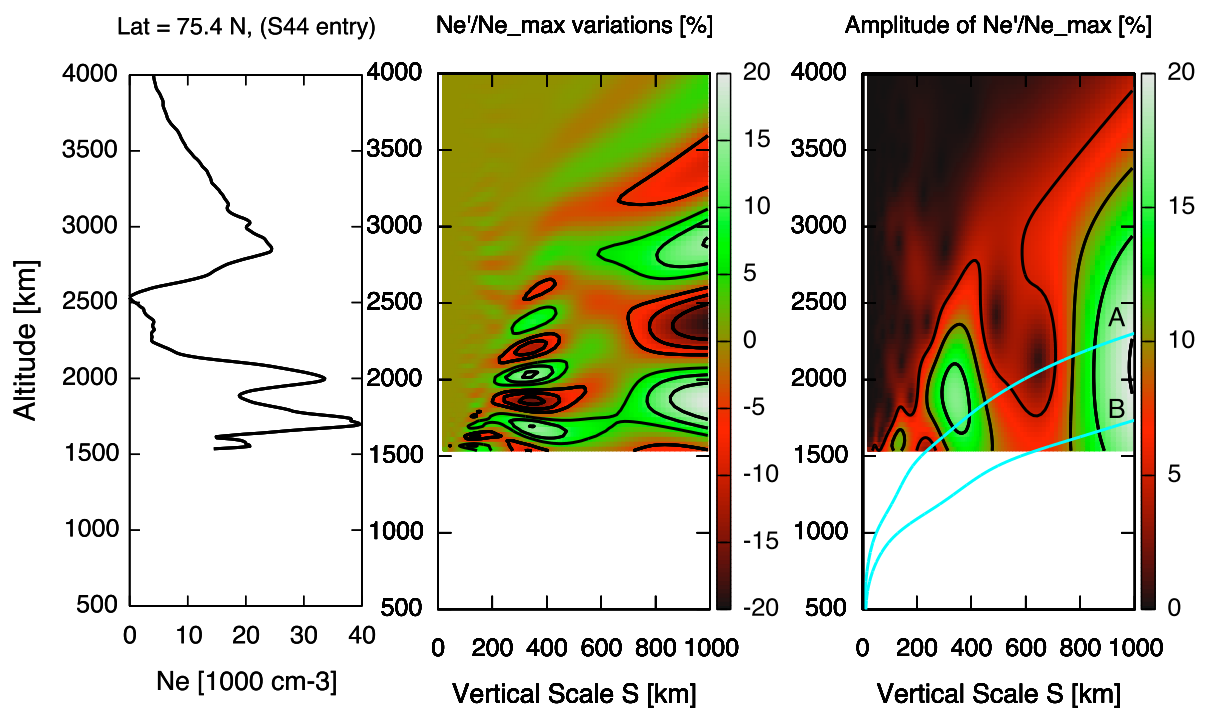


Figure A.12: As in Fig. 1, but for the high latitude observation at  $75.4^\circ\text{N}$  from S44 entry radio occultation.

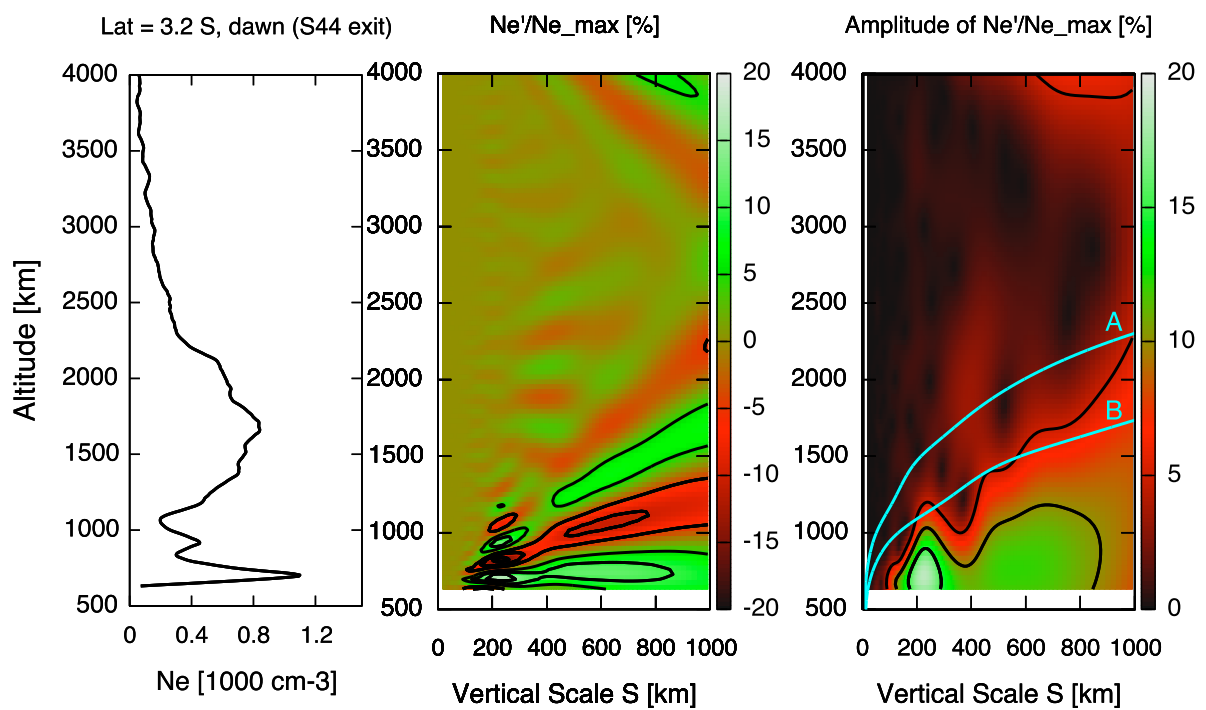


Figure A.13: As in Fig. 1, but for the low latitude dawn observation at  $3.2^\circ\text{S}$  from S44 exit radio occultation.

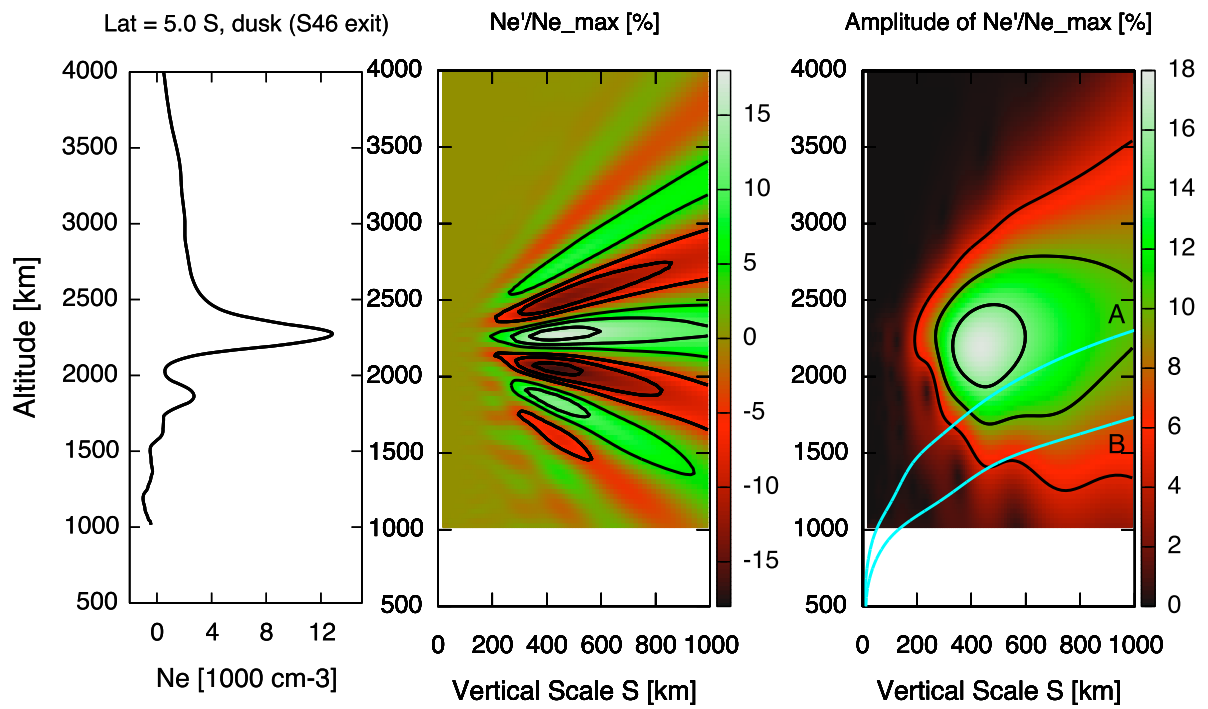


Figure A.14: As in Fig. 1, but for the low latitude dusk observation at  $5.0^\circ S$  from S46 exit radio occultation.

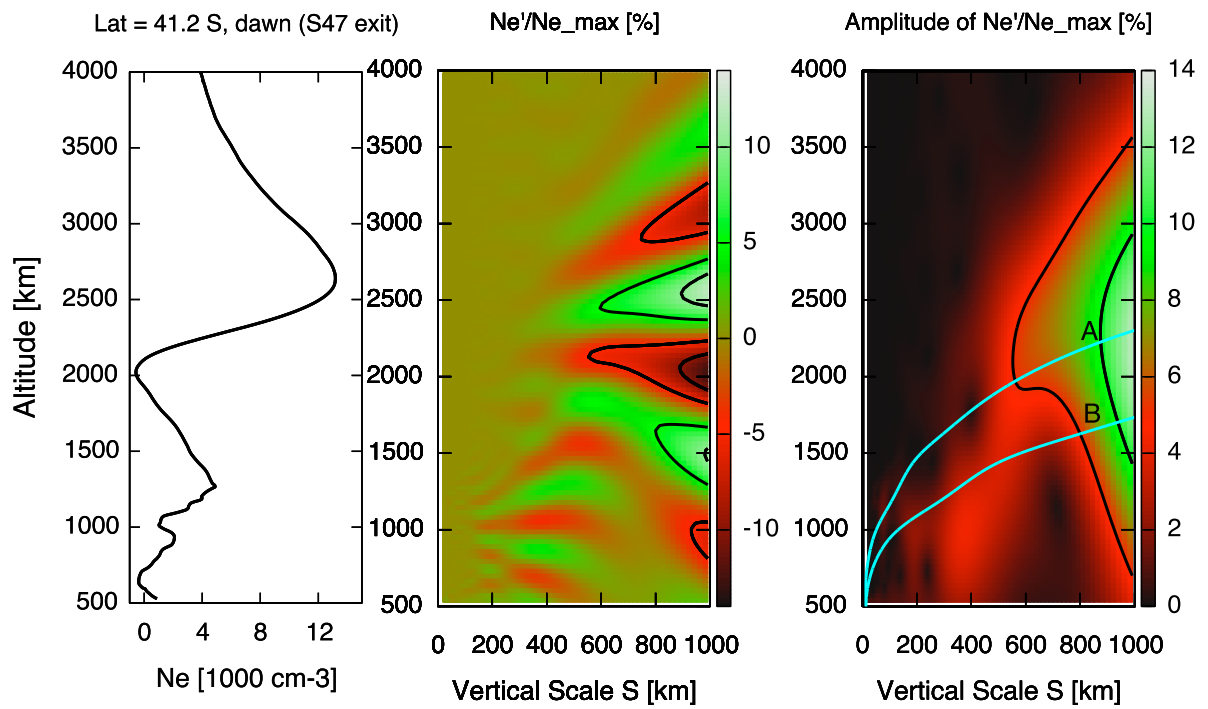


Figure A.15: As in Fig. 1, but for the middle latitude dawn observation at 41.2°N from S47 exit radio occultation.

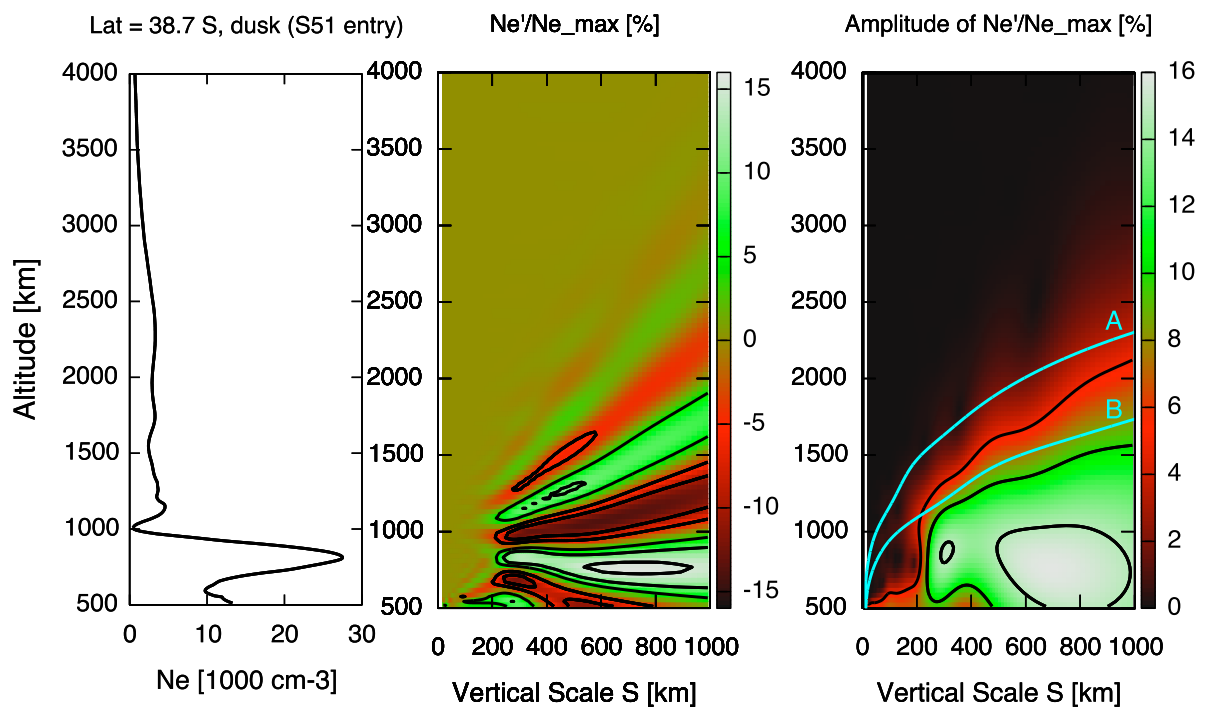


Figure A.16: As in Fig. 1, but for the middle latitude dusk observation at 38.7°S from S51 entry radio occultation.

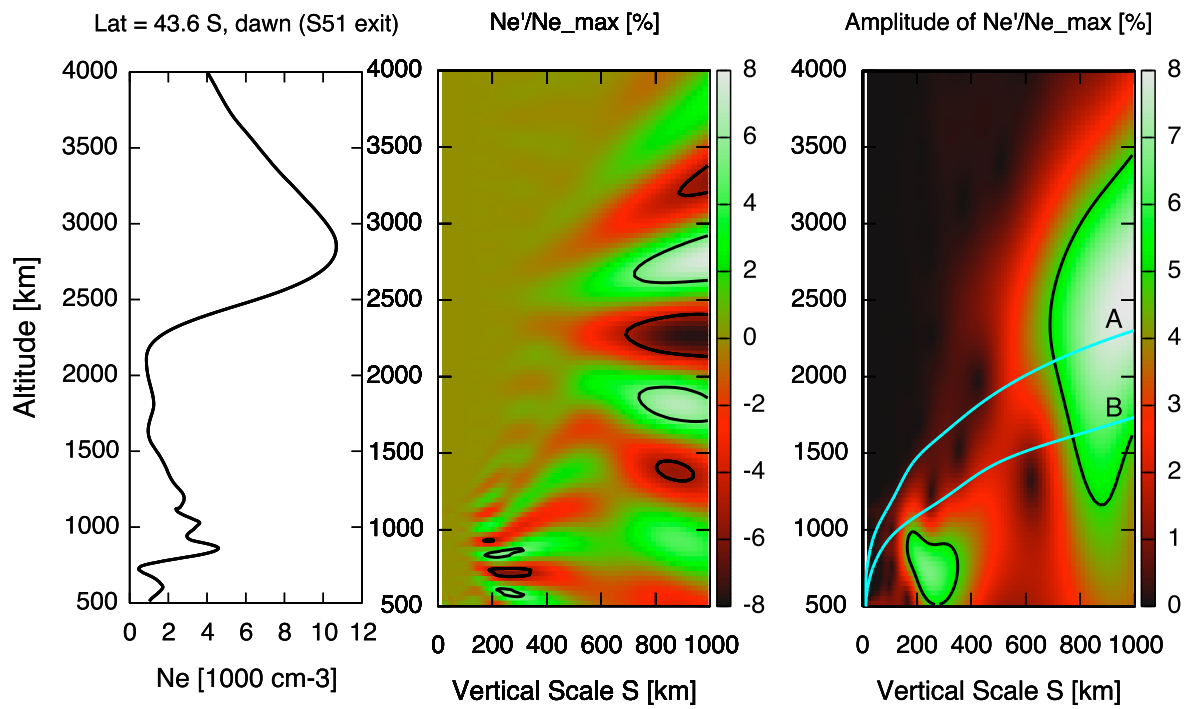


Figure A.17: As in Fig. 1, but for the middle latitude dawn observation at  $43.6^\circ\text{S}$  from S51 exit radio occultation.

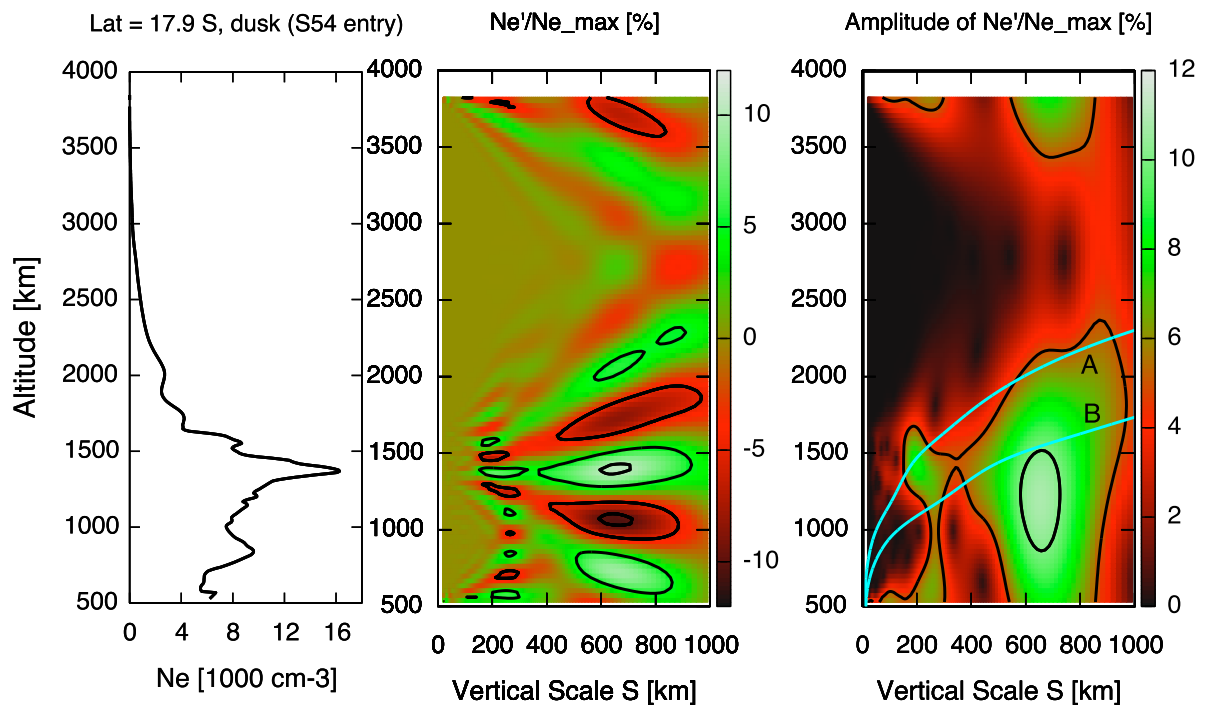


Figure A.18: As in Fig. 1, but for the low latitude dusk observation at 17.9°S from S54 entry radio occultation.

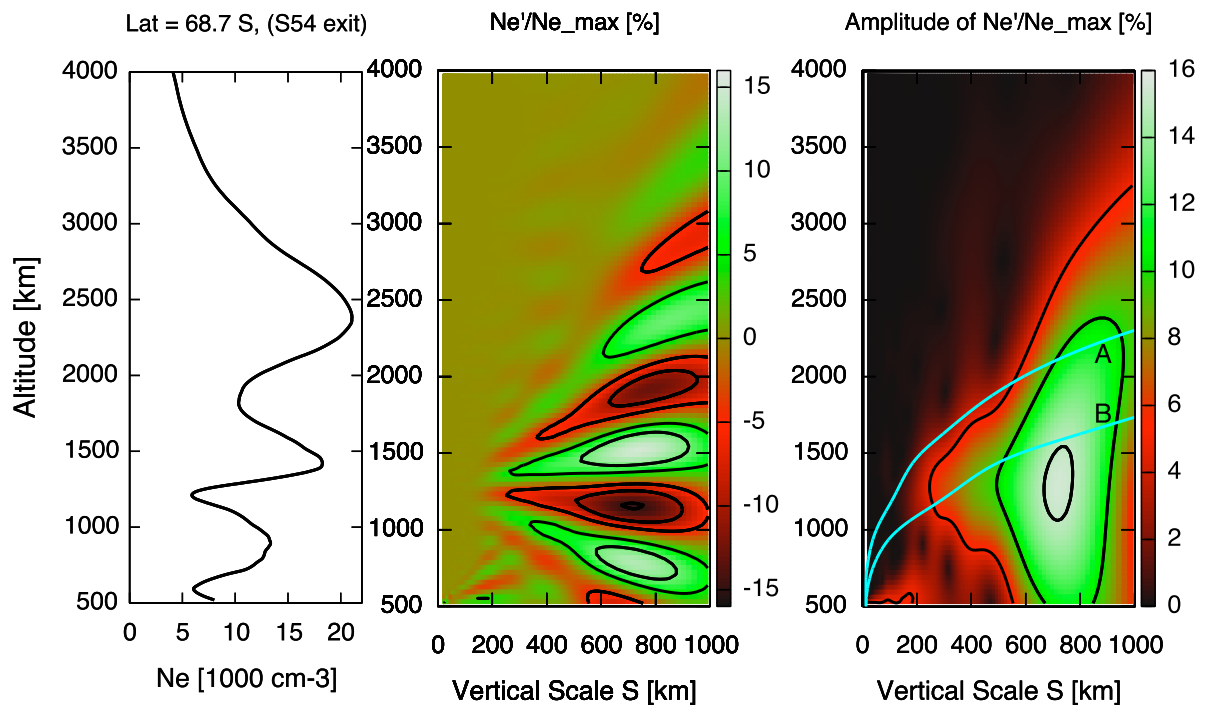


Figure A.19: As in Figure 1, but for the high latitude observation at 68.7°S from S54 exit radio occultation.

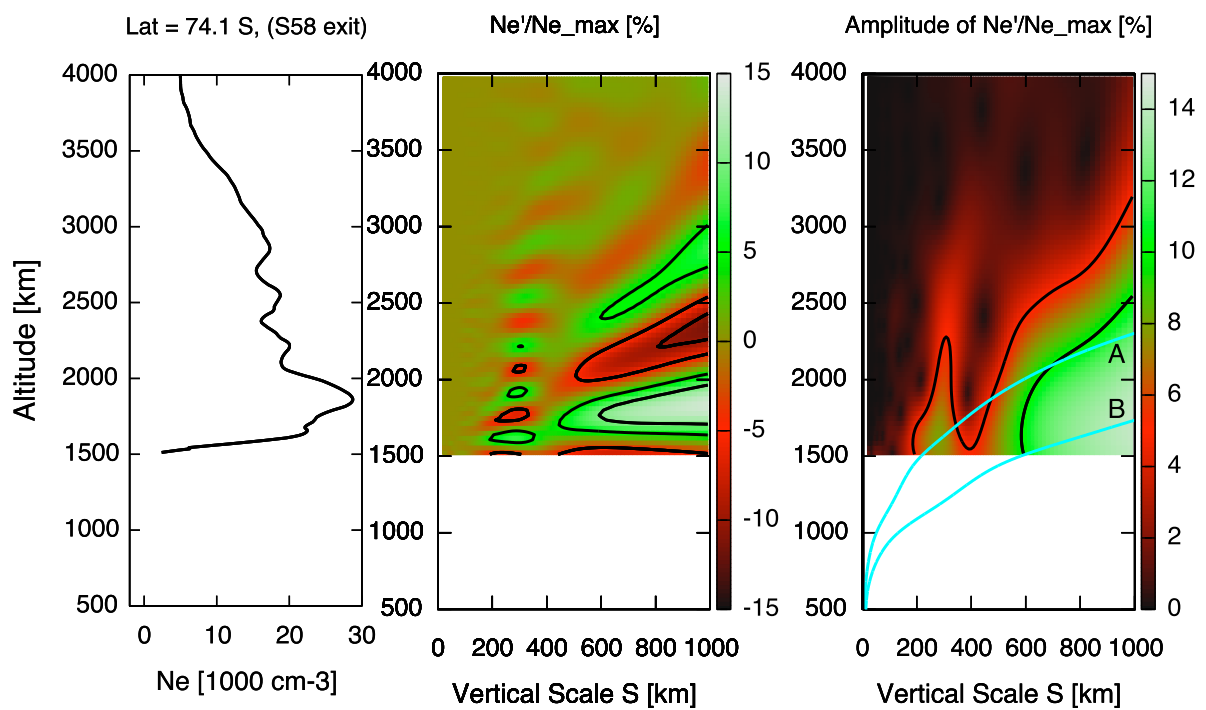


Figure A.20: As in Figure 1, but for the high latitude observation at 74.1°S from S58 exit radio occultation.

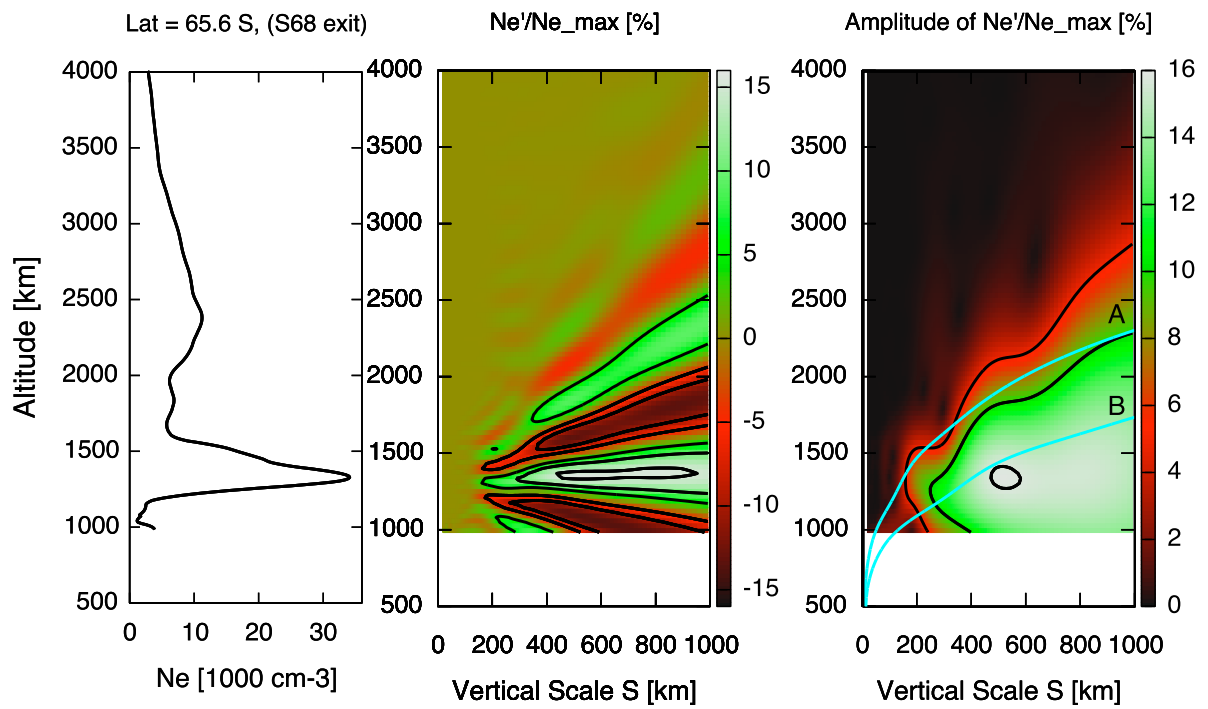


Figure A.21: As in Figure 1, but for the high latitude observation at 65.6°S from S68 exit radio occultation.

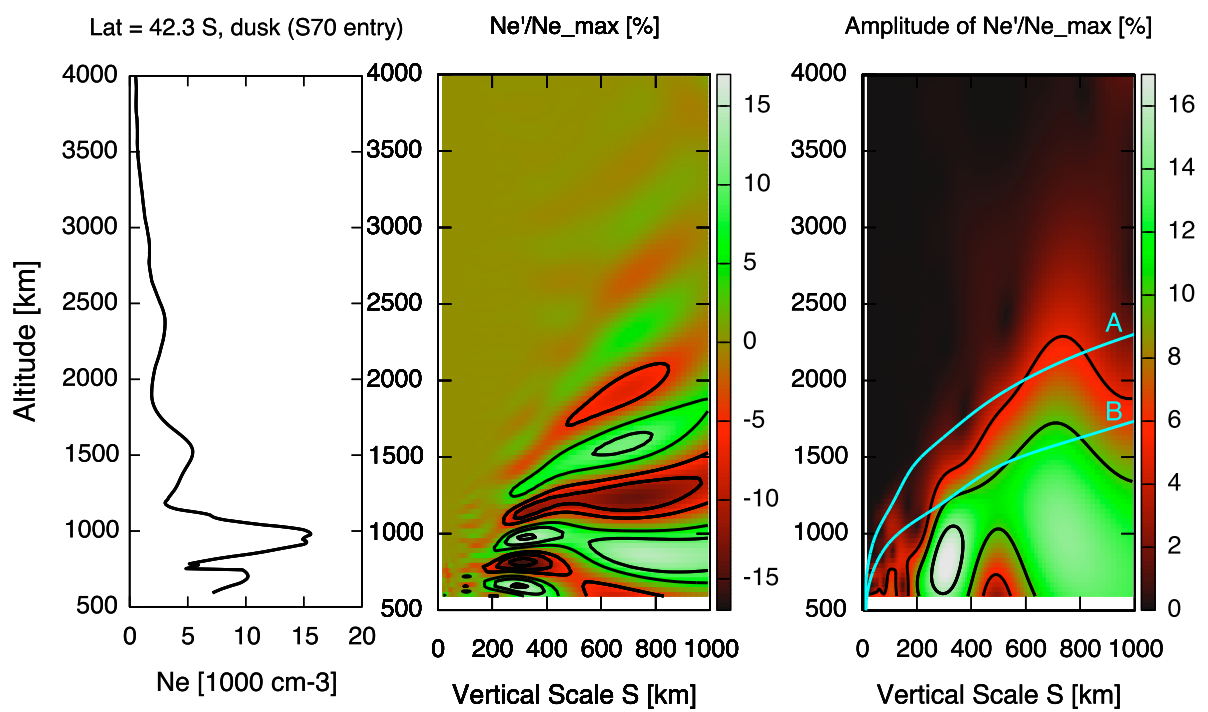


Figure A.22: As in Fig. 1, but for the middle latitude dusk observation at 42.3°S from S70 entry radio occultation.

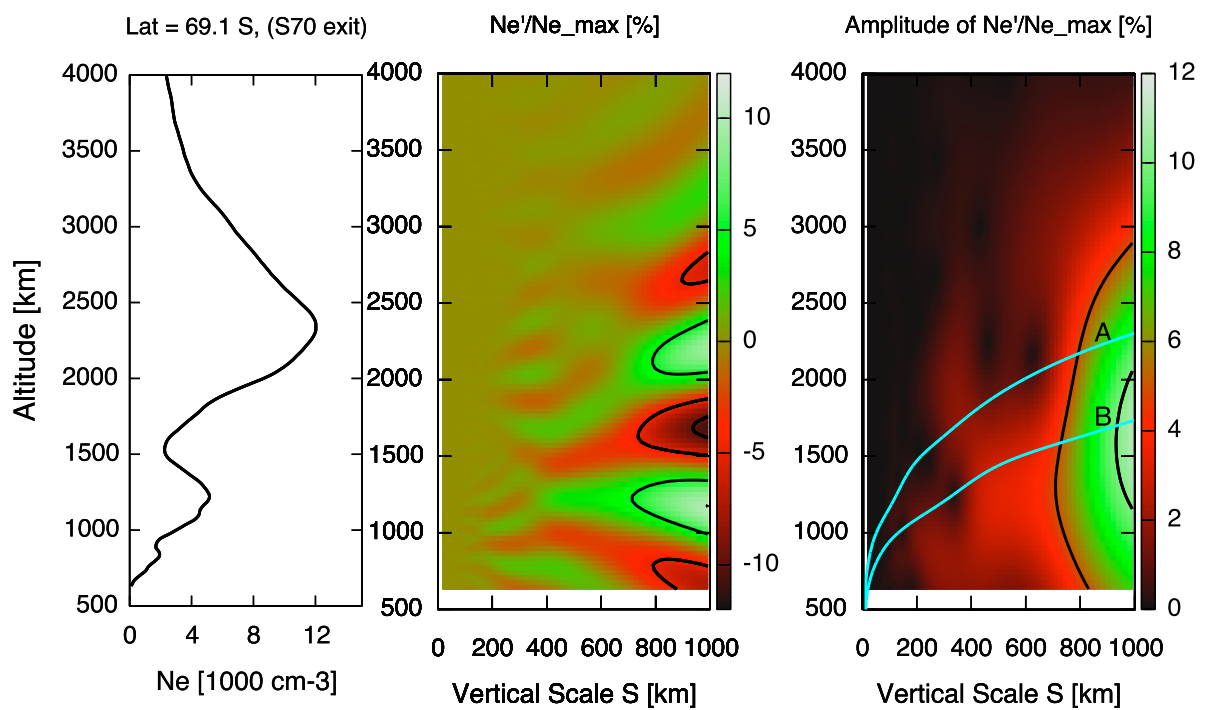


Figure A.23: As in Fig. 1, but for the high latitude observation at 69.1°S from S70 exit radio occultation.

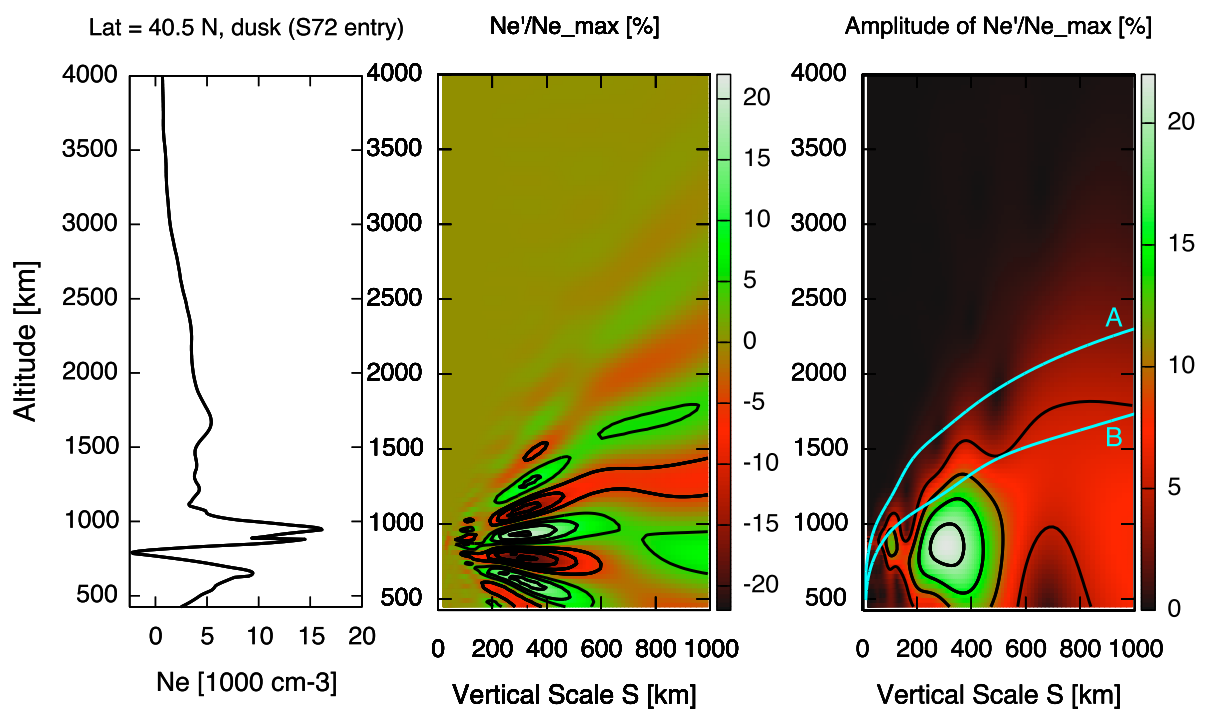


Figure A.24: As in Fig. 1, but for the middle latitude dusk observation 40.5°N from S72 entry radio occultation.

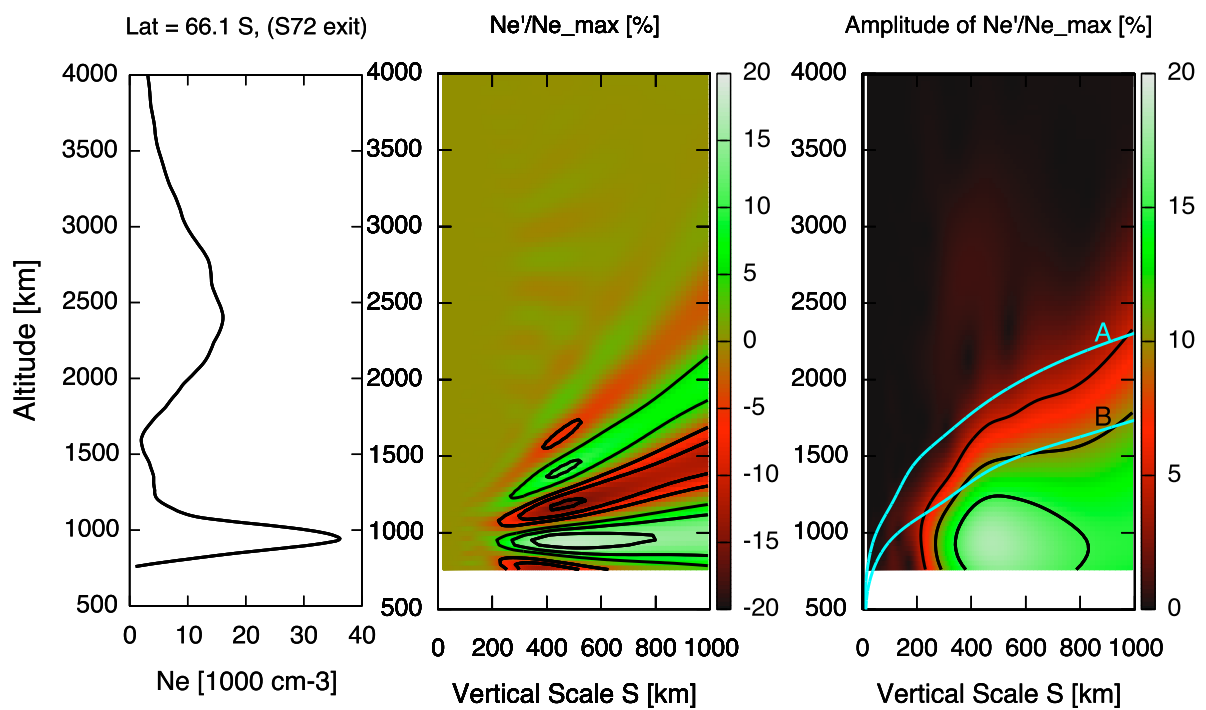


Figure A.25: As in Fig. 1, but for the high latitude observation at 66.1°S from S72 exit radio occultation.

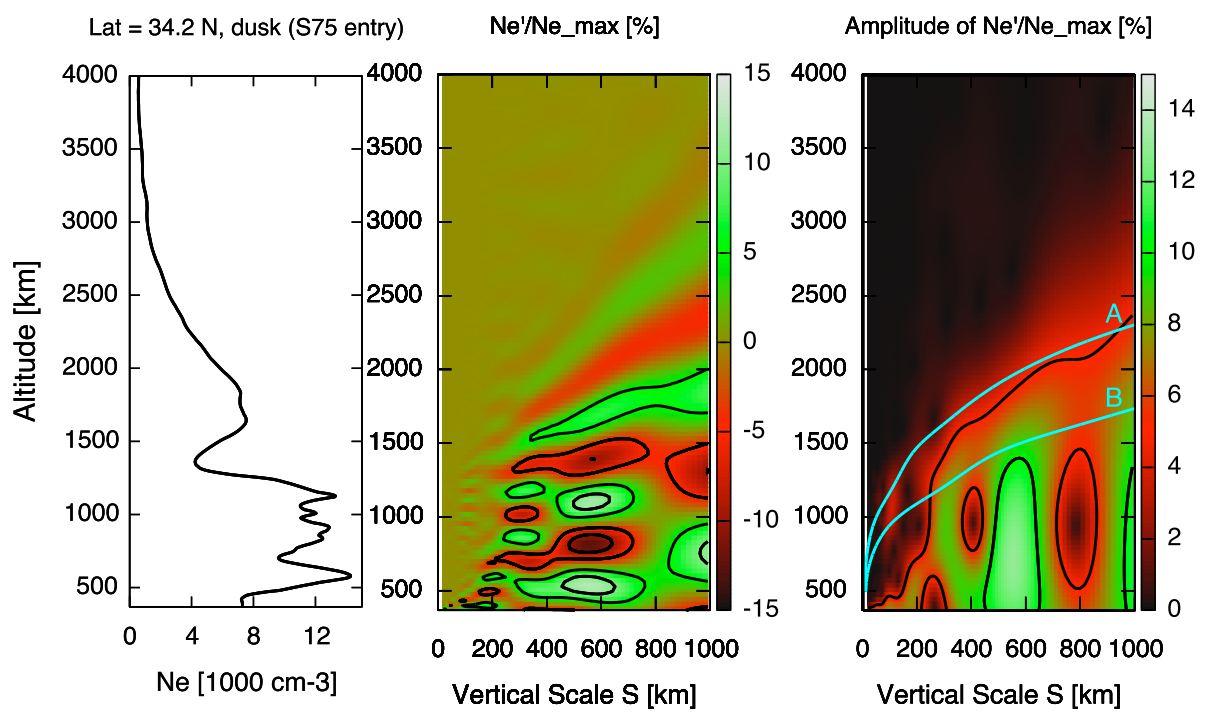


Figure A.26: As in Fig. 1, but for the middle latitude dusk observation at 34.2°N from S75 entry radio occultation.

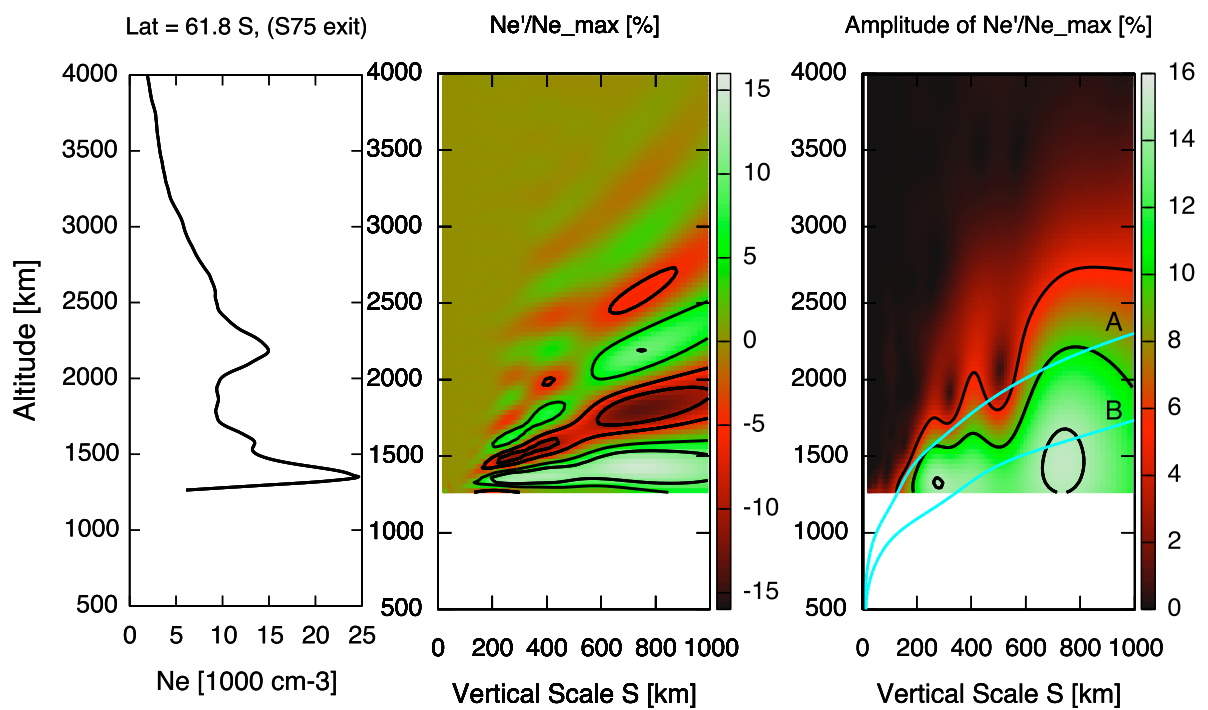


Figure A.27: As in Fig. 1, but for the high latitude observation at 61.8°S from S75 exit radio occultation.

### Highlights

- We perform a wavelet analysis on 31 Cassini Electron density profiles.
- Virtually all profiles at all latitudes show significant variability at 250 to 450 km scale.
- Overall the most often observed vertical scale is 300 km.
- The spectral characteristics of the observed variability are consistent with atmospheric gravity waves being the underlying driving mechanism.

ACCEPTED MANUSCRIPT